Elucidating the nature role of acid etching on the CoMnOx catalyst with outstanding performance for the catalytic combustion of o-dichlorobenzene

Shixing Wu [a,b], Shilin Wu [c], Fang Dong [a], Yuntai Xi [a,d], Peng Wang [c], Yinghao Chu [c], Zhicheng Tang [a,e,*], Jiyi Zhang [d]

[a] National Engineering Research Center for Fine Petrochemical Intermediates, State Key Laboratory for Oxo Synthesis and Selective Oxidation, Lanzhou Institute of Chemical Physics, Chinese Academy of Sciences, Lanzhou 730000, PR China
[b] University of Chinese Academy of Sciences, Beijing 100039, PR China
[c] College of Architecture and Environment, Sichuan University, Chengdu 610065, PR China
[d] School of Petroleum and Chemical, Lanzhou University of Technology, Lanzhou 730050, China
[e] Shandong Laboratory of Advanced Materials and Green Manufacturing at Yantai, Yantai Zhongke Research Institute of Advanced Materials and Green Chemical Engineering, Yantai 264006, China

ARTICLE INFO

ABSTRACT

Enhancing chlorine and water resistance and suppressing by-product generation are crucial issues in the catalytic degradation of CVOCs. In this paper, surface acid modified (sulfurized and phosphorized) CoMnOx rhombic dodecahedra catalysts were synthesized for the deep destruction of o-Dichloroethane (o-DCB), considering its better reducibility, abundant acid sites, excellent mass transfer and higher specific surface area. The strong interaction between Co and Mn in the acid-modified CoMnOx stimulated the efficient production of active Co^{3+}, Mn^{4+} and oxygen species, which considerably promoted C-H bond and C-Cl bond cleavage. Acid etching also creates a rich surface defect structure that promotes the exposure of more reactive sites and facilitates the adsorption of reactant molecules. Furthermore, we found that the acid sites of the prepared CoMnOx-TAA materials effectively inhibited by-product formation and were highly selective for HCl. TPSR analysis gave the distribution of the reaction products and further confirmed that the final products were CO_2 and HCl. More importantly, CoMnOx-TAA exhibited excellent water and chloride resistance. Moreover, EPR characterization confirmed a significant increase in the number of oxygen vacancies on the catalyst surface after acid modification of CoMnOx. TPD indicated that the modified catalyst possessed abundant weak and medium acid sites. The formation pathway and reaction mechanism of oxidative decomposition were also studied by in-situ FTIR and DFT calculations. This work provides promising candidates and new insights into the industrial catalytic degradation of o-DCB.

1. Introduction

Chlorinated volatile organic compounds (CVOCs) are a class of air pollutants with bioaccumulation potential, high toxicity, long persistence, high chemical stability and strong carcinogenicity, which have significant negative impacts on human health and the natural environment [1]. CVOCs are known to be a precursor of O_3. When O_3 is present in high concentration for a long time, it is easy to cause photochemical smog which is harmful to the environment [2]. Therefore, some countries have implemented strict environmental regulations for the emission of CVOCs [3,4]. o-DCB is a typical CVOCs, mainly from the

petrochemical, medical device manufacturing, coating, vinyl chloride (VC) production, printing process and metal degreasing industries [3]. Currently, there are numerous methods to control and reduce CVOCs, among which catalytic combustion is considered one the most promising and effective pathways [4,5]. Catalytic oxidation, with its advantages of high selectivity, more economic advantages, low organic by-products, low operating temperature and low energy consumption, is widely regarded as one of the most effective technologies for the decomposition of CVOCs [6,7].

Nowadays, most of the reported catalytic materials mainly involve zeolites, noble metals or non-precious metal oxides [3,5,7]. For zeolite

materials, the original activity is not ideal and can also lead to denaturation and deactivation due to coke deposition [3,8]. Normally, noble metals involved in the industry such as Rh, Pd, Ru and Pt based catalysts have high activity for catalytic combustion of CVOCs, but they are prone to chlorine poisoning which causes catalyst deactivation, and also easy to form more toxic substances like dioxins [8]. Noble metals are sensitive to inorganic chlorine formed during the catalytic decomposition of CVOCs, so they are more selective for chlorination reactions [8,9]. For transition metal oxides, although the activity is generally lower than that of noble metal catalysts, their chlorine poisoning resistance is significantly stronger [4,10]. Transition metals such as Co, Fe, Cu, Cr, Mn and V-based catalysts have excellent chlorine poisoning resistance and are commonly used for the catalytic decomposition of CVOC [1,5, 11].

Cobalt-based catalysts are very easy to produce active oxygen species and have excellent bulk mobility and relatively low O_2 vaporization enthalpy, so they have outstanding activity for the oxidative decomposition of CVOCs [12,13]. Co-based catalyst materials doped with other metals to improve the activity of the catalyst have been deeply studied. Metal dopants can change the electronic and geometric properties of metal oxides and the strong interaction between metals to affect the active oxygen species on the catalyst surface [8,14,15]. For example, Wang et al. reported that the introduction of Co into Ru/Al_2O_3 greatly improved the mobility of active oxygen species, and the strong interaction between metals could accelerate the electron transfer of the active site of the catalyst and improve the catalytic activity of vinyl chloride degradation [16,17]. In our previous experiment, we reported that $CoCuO_x$ with core-shell structure had excellent C-Cl dissociation activity, reducibility and chlorine poisoning resistance, and had high activity for oxidative decomposition of chlorinated aromatic hydrocarbons [18].

CVOCs have special physical and chemical properties, so it is difficult for single-component catalysts to meet the requirements of stability, selectivity, water resistance and low-temperature activity at the same time. Therefore, the influence of the surface acidity of the catalyst on the catalytic combustion of CVOCs has been widely concerned. The surface acidity of catalytic materials has an important influence on the distribution of oxidation decomposition products of CVOCs [19,20]. Generally speaking, the acid site of the catalyst is divided into Lewis acid and Brønsted acid [20,21]. The cleavage of C-Cl bond is related to the Lewis acid site, while the Brønsted acid site provides sufficient H proton to combine with Cl to generate HCl, which promotes the resolution of Cl species. The intermediate products in the catalytic reaction process are oxidized to CO_2 at other active sites or Lewis acid sites [22,23]. According to several researchers, the Brønsted acid site promotes the conversion of species that poison the catalyst with chlorine into HCl during catalytic oxidation. This successfully prevents chlorine poisoning of the catalyst and increases stability [24]. The Brønsted acid site can promote proton shuttle, which is conducive to the formation of HCl, and HCl will be desorbed [20,24,25]. Wang et al. pointed out that the oxidative decomposition of dichloromethane on the acid-modified catalyst occurs by adsorption on the surface acid site, which first causes the C-Cl bond to break, then gradually turns the oxide into CH by-product, and finally into CO_2 [11,26,27]. Liu et al. investigated the effect of surface acidity on the redox performance of the catalyst, which further affected the oxidative decomposition of vinyl chloride [27]. Proper treatment of the catalyst with acid is an effective way to increase the number of defects on the surface of the catalyst, and enhance the oxidation and reduction performance of the catalyst [28–30].

To this end, we have successfully carried out acid modification of $CoMnO_x$ dodecahedron (surface phosphorylation and sulfurization). We found the modified catalysts had excellent activity and superior stability over the pristine $CoMnO_x$. More importantly, the selectivity of chlorinated by-products on the modified catalysts was significantly suppressed. Additionally, various parameters of the prepared $CoMnO_x$ and modified catalysts ($CoMnO_x$-AP, $CoMnO_x$-TAA and $CoMnO_x$-S) were

investigated, including catalytic oxidation activity, selectivity, water resistance, apparent activation energy, thermal stability, morphology, redox ability, acid sites and recycling performance. Detailed characterization unveils the potential mechanisms underlying the outstanding catalytic performance of the synthesized samples. Therefore, the differences in the catalytic oxidation of o-DCB by modified catalysts were comparatively investigated based on surface acidity-regulated catalytic systems to achieve efficient decomposition of typical pollutants o-DCB.

2. Experimental

2.1. Synthesis of CoMn-ZIFs and CoMn/C

Dissolve 1.311 g $Co(NO_3)_2 \cdot 3\ H_2O$ and 0.502 g $Mn(NO_3)_2 \cdot 4\ H_2O$ in 60 mL methanol to form A solution. Then 0.048 mol of 2, 4-Dimethylimidazole (2-MIM) was dissolved in 40 mL of methanol to form solution B. Stir for 25 min, quickly mix A and B, and stand for 24 h at normal temperature. The sediment is collected by centrifugation, washed with methanol several times, and then dried at 80 °C, and the as-prepared precipitate is named as CoMn-ZIFs. Put CoMn-ZIFs into a tubular furnace and carbonize for 2.5 h at 400 °C under a nitrogen atmosphere to obtain CoMn/C (Scheme 1).

2.2. Synthesis of modified catalysts (CoMnO$_x$-AP, CoMnO$_x$-TAA and CoMnO$_x$-S)

The samples treated by ammonium phosphate (AP), thioacetamide (TAA) and H_2SO_4 were recorded as $CoMnO_x$-AP, $CoMnO_x$-TAA and $CoMnO_x$-S, respectively. For $CoMnO_x$-AP, the required amount of (molar ratio of P/CoMn controlled at 0.1) AP was dissolved in 10 mL of deionized water. Afterward, 1.0 g of CoMn/C was added to the above solution and the subsequent operation was carried out for the CoMn/C sample. The precipitate obtained by centrifugation was washed several times with methanol and dried at 60 °C for 10 h. For $CoMnO_x$-TAA, 0.488 g of TAA was added to a solution containing 40 mL of ethanol and 25 mL of ultrapure water. 1.0 g of CoMn/C was added to the above solution after thorough stirring. The mixture was stirred vigorously for 1 h, and it was centrifuged and dried. For $CoMnO_x$-S, immerse 2.5 g of CoMn/C in 20 mL (0.5 mol/L) of H_2SO_4 solution at 35 °C. Then wash the product thoroughly and dry the solid obtained by centrifugation at 120 °C overnight (Scheme S1).

All materials obtain above were calcined at 450 °C for 3 h with a rate of 1 °C/min.

2.3. Catalyst characterizations

We have characterized the catalytic materials using EPR, BET, FT-IR, TG-DSC, Raman, XRD, FE-SEM, HR-TEM, EDS-mapping, TPSR, XPS, NH_3-TPD, H_2-TPR, O_2-TPD, DFT calculation and in-situ FTIR, the detailed procedures of which are described in the supporting information.

2.4. Activity measurement

The sample preparation and procedures for the o-DCB catalytic performance process are embodied in the supporting information.

3. Results and discussion

3.1. Physical properties of the synthesized catalysts

Fig. S1 and Table 1 show the specific surface (S_{BET}) and pore structure of prepared $CoMnO_x$ and modified catalysts ($CoMnO_x$-AP, $CoMnO_x$-TAA and $CoMnO_x$-S) materials. In the relative pressure range of 0.5–1.0, all four catalysts exhibit a classical hysteresis loop, this belongs to the type IV isotherm, which is associated with the formation of massive
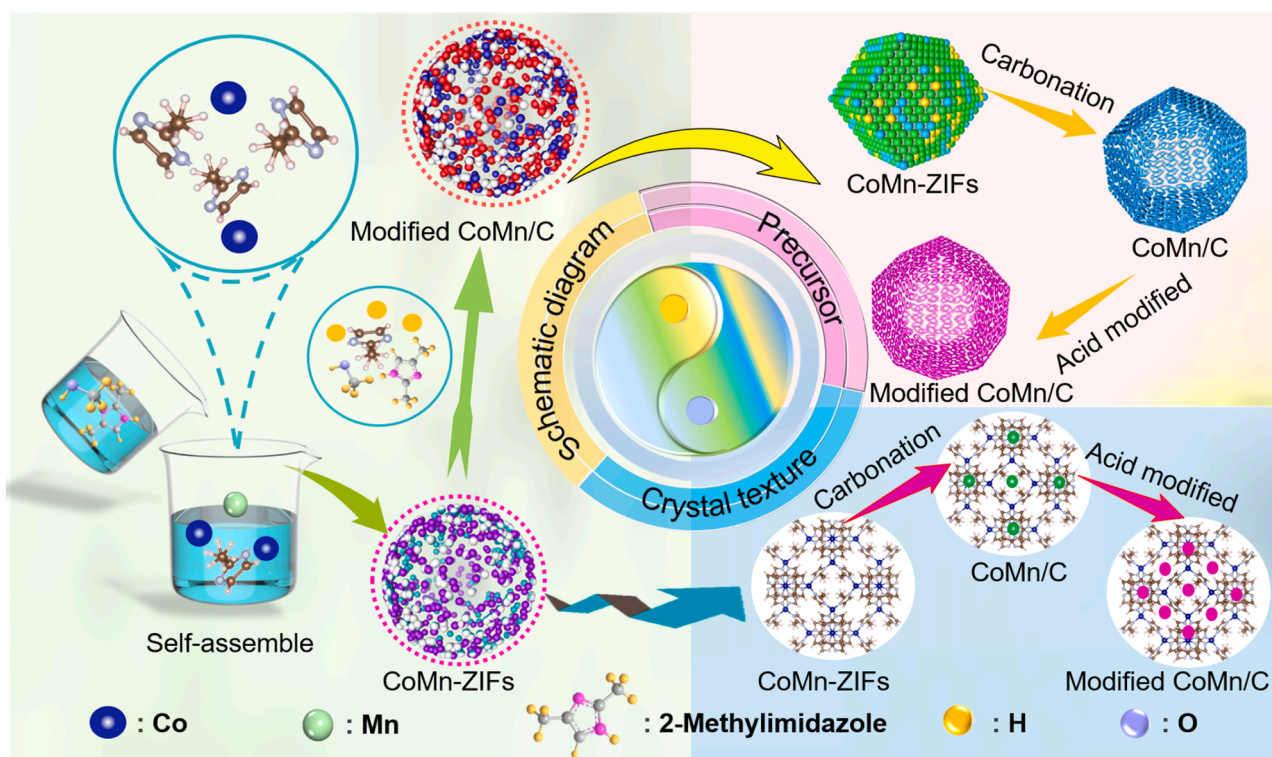
Scheme 1. Schematic diagram of the synthesis process for $CoMnO_x$ and modified catalysts.

Table 1
BET test results of prepared $CoMnO_x$ and modified catalysts.

Catalysts	Surface area (m^2 g^{-1})[a]	Pore size (nm)[b]	Pore volume (cm^3 g^{-1})[c]
$CoMnO_x$	104.41	7.41	0.29
$CoMnO_x$-AP	144.79	7.07	0.28
$CoMnO_x$-TAA	162.79	6.38	0.30
$CoMnO_x$-S	138.42	7.45	0.31

[a] Determined by BET surface area.
[b] Determined by desorption branch.
[c] Adsorbed volume at $P/P_0 = 0.992$.

mesoporous structures [18,26]. Table 1 also summarizes the S_{BET}, pore size volume and pore volume of the catalysts. The S_{BET} of the pristine $CoMnO_x$ is the smallest compared to the modified catalyst, which is primarily due to particle agglomeration. For the acid-treated modified catalysts, the S_{BET} increases significantly, and this structural property is critical for significantly increasing reactant accessibility to active sites. High S_{BET} promotes the dispersion of active components and can provide sufficient adsorption sites for the reactants during the o-DCB catalytic decomposition process [28]. Combined with the catalytic performance test, the specific surface area of $CoMnO_x$-TAA catalyst not only increased significantly but also had the best catalytic activity, indicating that the specific surface area plays a key role in o-DCB catalytic combustion.

Fig. 1a and Fig. S2 displays wide-angle XRD patterns of $CoMnO_x$ and modified catalysts. For prepared catalysts, four peaks appear at 19.00, 36.85, 38.55 and 77.34° are attributed to Co_3O_4 spinel structure (JCPDS 43–1003) [18,29]. The material exhibits the diffraction peaks at 31.26, 36.82, 44.83, 55.77, 59.47 and 65.34°, corresponding to the (220), (311), (400), (422), (511) and (440) planes of the spinel $Co_2MnO_{4.5}$ phase (JCPDS 32–0297), suggesting the presence of Co and Mn in the form of composite oxides [31]. For the $CoMnO_x$-AP catalyst, a weak diffraction peak appears at 23.21°, ascribed to a porous CoP_4 dodecahedron (JCPDS 20–0036). Surprisingly, no other diffraction peaks were

found in the XRD spectrum of the sulfurized material, indicating that the inherent characteristics of CoMn/C after sulfurization did not change significantly. After the acid modification treatment, the diffraction peak intensities were all lower, indicating that the crystallinity and morphology of the catalysts had changed. Moreover, this also indicates the presence of lattice distortion and strong interaction between Co and Mn in the acid-modified catalyst, which contributes to the enhancement of catalytic activity.

When the pristine $CoMnO_x$ was modified with acid, the EPR signal intensity was significantly enhanced, indicating a significant increase in the number of oxygen vacancies on the surface of the modified catalyst (Fig. 1b and Fig. S3). The prepared catalysts only show a significant response at g= 2.003, mainly attributed to electron capture at the oxygen vacancies on the catalyst surface. Additionally, there are different concentrations of oxygen vacancies in the modified catalysts due to differences in the type and acidic strength of the acids used for modification. For $CoMnO_x$-TAA, a significantly enhanced signal was observed at g= 2.003, which indicates that this sample contains an abundance of oxygen vacancies corresponding to the electron capture of oxygen defects. A high number of oxygen vacancies can significantly enhance the interaction between the composite metal oxides, thus improving the thermal stability of the dispersed metal species. Correspondingly, oxygen vacancies can modulate the electronic structure of the catalyst surface and promote the generation of more adsorption and active sites, thereby improving catalytic performance. Therefore, the excellent catalytic oxidation performance of $CoMnO_x$-TAA benefits from a large extent from the abundance of oxygen vacancies.

On Raman spectrum (Fig. 1c and Fig. S4) of $CoMnO_x$ and modified catalysts, several Raman peaks at 181, 470, 514, 618 and 674 cm^{-1} correlate to various modes of the Co_3O_4 phase [32]. Among them, the peaks at 470 and 514 cm^{-1} could be considered as the E_{2g} and $F_{2g'}$ symmetry. The peaks at 181 and 618 cm^{-1} are ascribed to the F_{2g} and $F_{2g'}$ symmetry modes of Co_3O_4 [32]. Furthermore, a strong peak is observed at 674 cm^{-1}, which is associated with the A_{1g} symmetry pattern of Co_3O_4 [32,33]. For the $CoMnO_x$-TAA catalyst, the peaks at
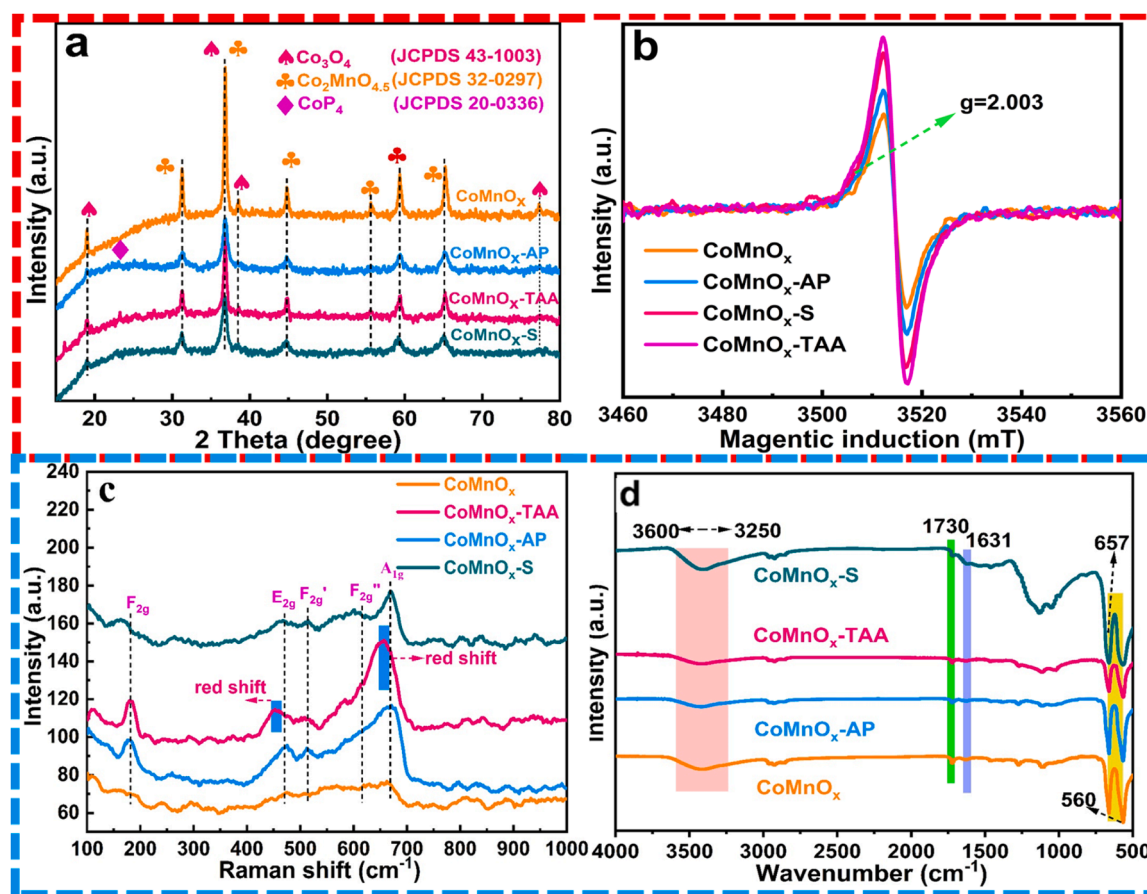
Fig. 1. (a) XRD profiles, (b) EPR spectra, (c) Raman spectra and (d) FTIR spectra of prepared materials.

470 and 674 cm^{-1} show a significant shift due to sulfurization, demonstrating that the lattice defects may be triggered by residual stress (Fig. S4). The obvious shift in the two Raman peaks of the CoMnO$_x$-TAA sample indicates the formation of abundant defect structures, which favor the formation of more active oxygen species and thus promote the conversion of o-DCB, in agreement with the results of XRD and catalytic properties (see later) [34,35].

Fig. 1d shows the FTIR spectra of the prepared samples. Stretching vibrations and bending peaks of physically adsorbed H$_2$O and surface hydroxyl groups (-OH) can be found in the 3600–3250 cm^{-1} interval for all catalysts [35]. The absorption peaks at 1631 cm^{-1} correspond to the stretching vibration peaks of physically adsorbed H$_2$O [5]. For all samples, a distinctive peak at 1730 cm^{-1} was observed, which was attributed to a mode of C=O stretching vibration [5,35]. In addition, two spikes can be observed at lower wavenumbers of 560 and 657 cm^{-1}, mainly attributed to the stretching vibrations of the Co^{2+}-O and Co^{3+}-O bonds, which are typical evidence for the presence of the Co-O group [18,35]. The FTIR characterization agrees with the XRD results (Fig. 1a).

### 3.2. TG-DSC, R$_s$ and R$_m$ analysis

The calcination of CoMn/C and modified CoMn/C was investigated by TG-DSC in Fig. S5a-d. Apparently, the weight loss of CoMn/C is classified into two main stages. The first mass loss (12.83%) occurs before 314 °C, which is primarily caused by residual water in the void space and the decomposition of structural water. The second mass loss is between 314 and 398 °C (34.12%), with a sharp exothermic peak caused primarily by the thermal decomposition of the metal skeleton. For the modified CoMn/C, the weight loss during the temperature rise was significantly higher than that of CoMn/C, which may be attributed to the decomposition of the sulfate remaining on the surface of the catalysts

with the temperature rise after the impregnation with acid solution. The results show that the organic matter in the catalyst is completely decomposed at 408 °C [18]. Furthermore, there was no further significant change in the mass loss curve after 408 °C, demonstrating that the sample was thermally stable [5]. As a result, the calcination temperature of the prepared material was set to 450 °C for 3 h. In addition, we determined the R$_s$ (reaction rates based on the specific area) and R$_m$ (reaction rates based on catalyst mass) of the produced samples to assess the catalytic efficacy based on the surface area (Fig. S5e-h). The R$_s$ values and R$_m$ of CoMnO$_x$-TAA were much greater than those of the other catalysts under the same conditions.

3.3. Morphology characteristics

Fig. 2 and Fig. S6 display the SEM and TEM images of prepared catalysts. Fig. 2a shows the SEM image of the precursor CoMn-ZIFs. We discovered that self-assembly was an effective method for preparing the homogenous and regular typical dodecahedron. The CoMn-ZIFs are well-dispersed and have a very smooth surface and are fairly neat, showing dodecahedra with a uniform size of approximately 1600 nm. However, the original form of CoMn/C changed significantly after the precursor was treated with acid (Fig. 2b-d). The surface of CoMn/C-AP has sunken, which is a folded surface structure with many pores and the surface becomes considerably rough, but it still maintains the structure of a dodecahedron (Fig. 2b). CoMn/C-TAA materials still maintain a well-dispersed dodecahedral structure with a relatively rough surface. Only a small portion of the materials exhibit sunken morphology, while the majority have corrugated morphology (Fig. 2c). Compared with other modified samples, the dodecahedral surface of CoMn/C-S is relatively smooth, but the polyhedral structure shrinks slightly (Fig. 2d). Fig. 2f-i and Fig. S7 exhibit TEM images of the four catalysts. After
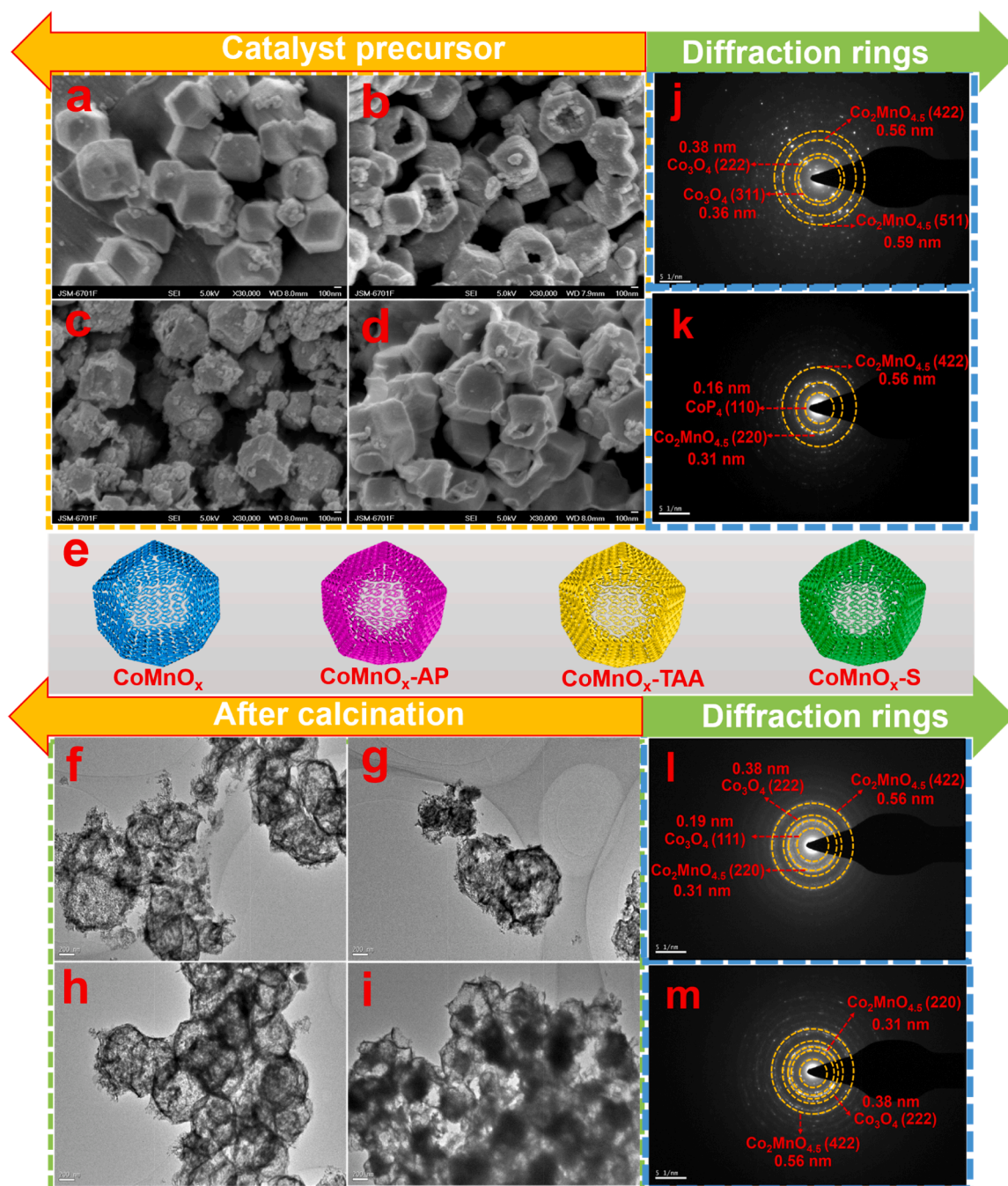
Fig. 2. FE-SEM images of (a) $CoMnO_x$, (b) $CoMnO_x$-AP, (c) $CoMnO_x$-TAA and (d) $CoMnO_x$-S; (e) 3D topography of prepared materials; TEM and diffraction rings of (f and j) $CoMnO_x$, (g and k) $CoMnO_x$-AP, (h and l) $CoMnO_x$-TAA and (i and m) $CoMnO_x$-S.

calcination, the sample still shows polyhedral morphology, the obvious difference is the collapse of the metal skeleton structure and the depression of the dodecahedra confirms the formation of a hollow structure of the catalyst. From the SEM and TEM results, we observed changes in the pore structure of the CoMn/C dodecahedra after different acid treatments, which also indicated that the morphology of the CoMn-ZIFs polyhedra is completely under our control even when subjected to acid modification. Fig. 2j shows that the inter-planar distances of the $CoMnO_x$ sample are around 0.36 nm, 0.38 nm, 0.56 nm, and 0.59 nm, which correspond to the Co_3O_4 (311), Co_3O_4 (222), $Co_2MnO_{4.5}$ (422) and $Co_2MnO_{4.5}$ (511) planes, respectively. HRTEM of modified catalysts (Fig. 3k-m and Fig. S8) reveals inter-planar distances of 0.31 nm, 0.38 nm, and 0.56 nm, which correspond to the planes of $Co_2MnO_{4.5}$

(220), Co_3O_4 (222), and $Co_2MnO_{4.5}$ (422), respectively.

EDS-mapping was used to investigate the spatial distribution of Co, Mn, O and S in the $CoMnO_x$-TAA catalyst (Fig. 3a). A study of the element distributions reveals that these elements are epitaxially distributed on the dodecahedron, strongly overlapped and uniformly dispersed. The $CoMnO_x$-TAA material appears to have a porous and rough open surface, which enhances mass transfer and easier contact of the active metal phase with the reacting molecules. The good dispersion of these elements facilitated the exposure of the catalyst to a rich reaction surface, which is consistent with the results of the BET test. According to HRTEM pictures (Fig. 3b-e), all prepared catalysts had lattice fringes of $Co_2MnO_{4.5}$ and Co_3O_4, as demonstrated by the XRD results.
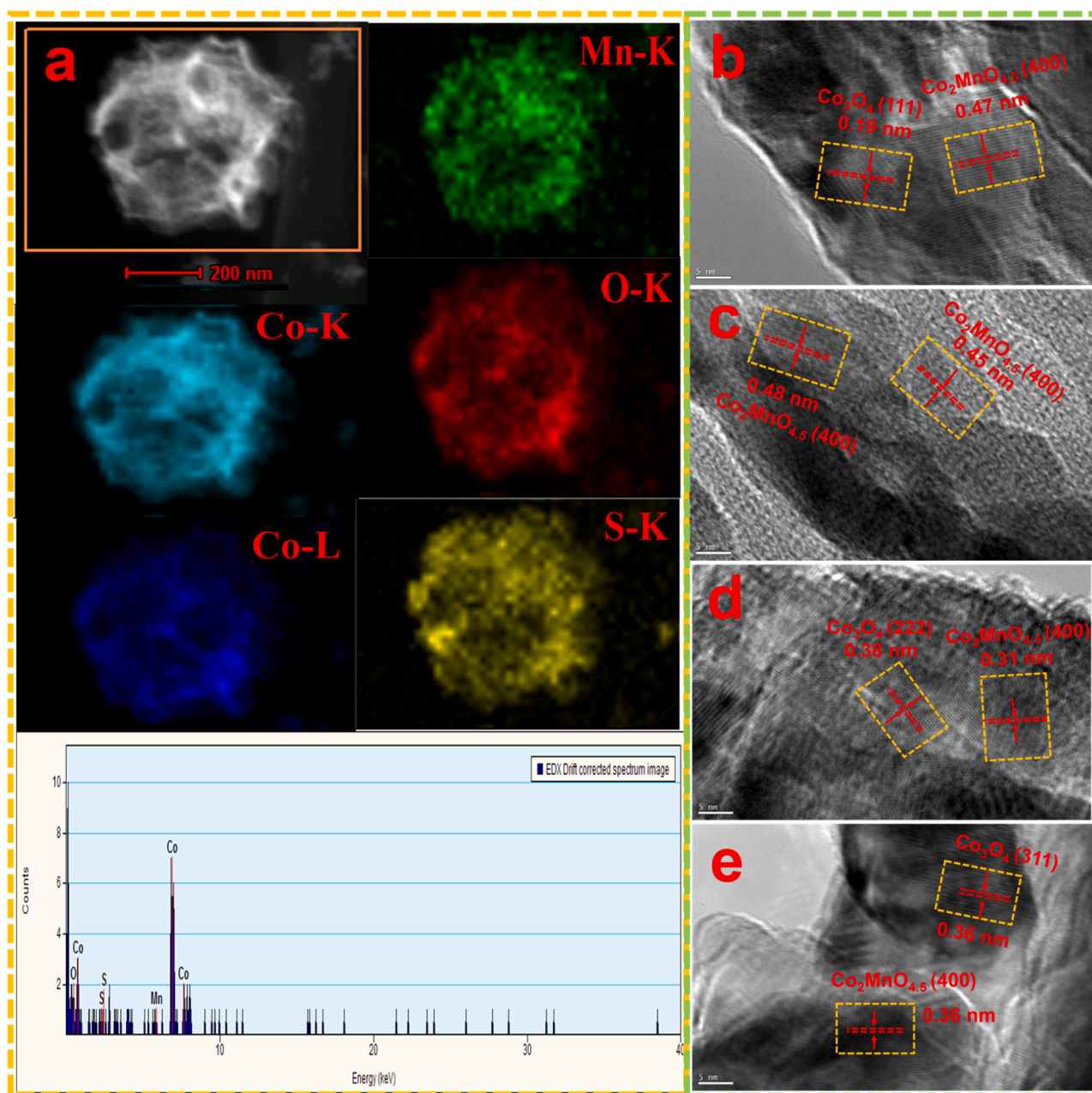
Fig. 3. Mapping analysis of (a) CoMnO$_x$-TAA. HR-TEM images of (b) CoMnO$_x$, (c) CoMnO$_x$-AP, (d) CoMnO$_x$-TAA and (e) CoMnO$_x$-S.

3.4. XPS analyses

Mn 2p, Co 2p, O 1 s, P 2p, S 2p and Cl 2p were studied using XPS, as presented in Fig. 4, Fig. S9 and Table 2. Co 2p spectra of all materials display two broad and asymmetric spin-orbit peaks centered at binding energies (BEs) of 780.3–781.6 and 795.2–796.6 eV, which are respectively attributed to Co 2p$_{3/2}$ and Co 2p$_{1/2}$ (Fig. 4a) [18,36]. The Co 2p$_{3/2}$ and Co 2p$_{1/2}$ spectra may further be separated into two different valence peaks for Co^{3+} and Co^{2+}. Surface Co^{3+} enables the catalyst to show excellent catalytic performance at lower temperatures [36,37]. Additionally, compared with the BE value of Co^{3+} and Co^{2+} in CoMnO$_x$, the BE value of Co^{3+} and Co^{2+} in modified catalysts is 0.2–0.5 eV and 0.1–0.4 eV higher, respectively. The shift of BE signifies that the electronic structure and distribution for Mn atom and Co atom are rearranged after being sulfurized and phosphated. The fresh CoMnO$_x$-TAA has a higher Co^{3+}/Co$_{total}$ content than the other samples, indicating that the synergistic interaction between the bimetals was exacerbated after

TAA treatment (Table 2). For the used CoMnO$_x$-TAA (labelled u-CoMnO$_x$-TAA), there was a significant decrease in the Co^{3+}/Co$_{total}$ content, suggesting that Co^{3+} is more active in the oxidative elimination of o-DCB (in agreement with the catalytic activity test). The abundance of Co^{3+} species facilitates the adsorption of gas molecules and also contributes to the formation of more active oxygen species [38].

Fig. 4b gives the Mn 2p$_{3/2}$ and Mn 2p$_{1/2}$ XPS curves of CoMnO$_x$ and modified catalysts, where two peaks are obtained by deconvoluting. The component at 641.75 ± 0.4 eV and 653.25 ± 0.5 eV are attributed to Mn^{3+} and that at 643.35 ± 0.5 eV and 654.45 ± 0.4 eV, to Mn^{4+} ions [33,39]. Because Mn^{4+} and Mn^{3+} perform an important role as electron acceptors and electron donors in the redox cycles with activate oxygen by electron transfer during catalytic combustion [40]. Furthermore, the following electron transitions occur between the Co and Mn cations: $2Co^{3+} + Mn^{2+} \rightarrow 2Co^{2+} + Mn^{4+}$ or $Co^{2+} + Mn^{3+} \rightarrow Co^{3+} + Mn^{2+}$, indicating a clear interaction between the Co and Mn cations, which is favorable to the combustion decomposition of o-DCB [5,40]. The
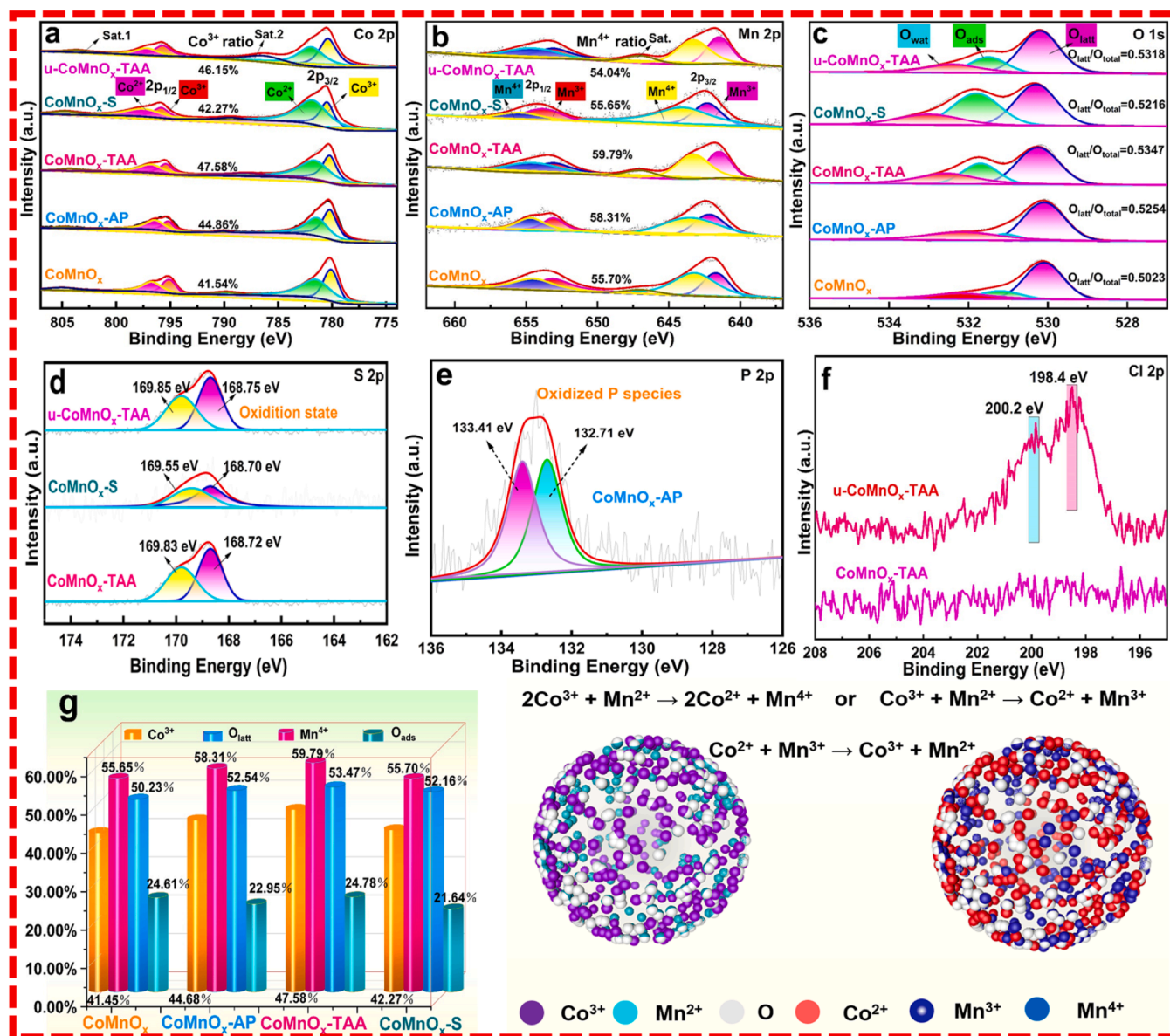
Fig. 4. XPS spectra of (a) Co 2p, (b) Mn 2p, (c) O 1 s, (d) S 2p, (e) P 2p and (f) Cl 2p. Interaction of (g) Co-Mn on surface of prepared catalysts and the relative proportion of catalysts active species.

Table 2
XPS data and surface acidity of synthesized CoMnOx and modified materials.

Catalysts	Co^{3+}/Co_{total} (%)	Mn^{4+}/Mn_{total} (%)	Mn^{3+}/Mn_{total} (%)	(Weak+Moderate)[a] peak areas	Strong[b] peak areas	O_{ads}/O_{total} (%)	O_{latt}/O_{total} (%)
CoMnOx	41.54	55.70	40.01	50.01	106.40	24.61	50.23
CoMnOx-AP	44.86	58.31	40.27	166.58	205.00	22.95	52.54
CoMnOx-TAA	47.58	59.79	39.57	437.61	131.00	24.78	53.47
CoMnOx-S	42.27	55.65	43.65	86.08	1888.00	21.64	52.16
u-CoMnOx-TAA	46.15	54.04	37.94	-	-	24.56	53.18

[a] Desorption peak areas of (weak+moderate) acid.
[b] Desorption peak areas of strong acid

CoMnOx-TAA sample possesses a high Mn^{4+}/Mn_{total} ratio due to sulfurization. The high Mn^{4+}/Mn_{total} molar ratio ensures the outstanding catalytic performance of CoMnOx-TAA for total o-DCB destruction in this study.

In terms of O 1 s species, the prepared catalysts contain three peaks at approximately 533.0–533.25, 531.25–531.75, and 530.05–530.35 eV, which are indexed to carbonates/adsorbed molecular water (O_{wat}), surface adsorbed oxygen (O_{ads}), and lattice oxygen labeled O_{latt} (Fig. 4c). The $O_{latt}/(O_{ads} + O_{latt})$ ratio was determined using the areas of O_{ads} and O_{latt} provided in Table 2. The order of $O_{latt}/(O_{ads} + O_{latt})$ ratio is CoMnOx-TAA > CoMnOx-AP > CoMnOx-S > CoMnOx. O_{latt} has a lower surface energy and higher mobility than O_{ads} and so operates as the active site of the catalyst involved in the oxidation of o-DCB [23,41,42].

Fig. 4d and Table S1 depicts the S 2p spectrum of the modified catalyst, with the peak at a BE of 168.65–168.75 eV attributable to S^{6+} [43]. The shoulder at BE = 169.45–169.85 eV shows the production of sulfate decorations on the catalyst surface [43]. The P 2p spectrum of the modified catalysts roughly ranging in 129.45–133.85 eV can be fitted as two components (Fig. 4e). The former is commonly referred to as a monodentate surface complex, whereas the latter is usually referred to as a PO_x species (bidentate surface complex) [44]. Fig. 4f exhibits the Cl 2p XPS of $CoMnO_x$-TAA and u-$CoMnO_x$-TAA catalysts. For u-$CoMnO_x$-TAA catalyst, two symmetric split peaks are observed at the positions of 200.2 and 198.4 eV, which could be ascribed to the 2p split peaks of Cl species [18]. Above results show that during the oxidative decomposition of o-DCB, Cl species are deposited on the catalyst surface, which causes a decrease in the activity or stability of the catalytic material.

Combining the XPS characterization results, we explored the Co-Mn interactions on the surface of the synthesized catalysts. As shown in Fig. 4g, the Mn^{4+} and Co^{3+} contents on the surface of the acid-treated catalysts were significantly increased. The increase in higher valence ions indicates that the acid modification triggered a strong interaction between Co^{2+}, Mn^{2+} and Mn^{3+}, favoring the production of many active metal species. The acid treatment leaves the catalyst surface in an unbalanced chemical state, which leads to the production of surface oxygen species or oxygen vacancies, which provide favorable conditions for the adsorption of gaseous oxygen. The results indicate that appropriate acid modification treatment can promote the generation of surface active oxygen and enhance the catalytic oxidation performance of the catalyst.

3.5. H_2-TPR, O_2-TPD and NH_3-TPD characterizations

Fig. 5a shows H_2-TPR profiles over $CoMnO_x$ at temperatures ranging from 100 to 800 °C. In general, CoO_x and MnO_x display distinct peaks in H_2-TPR measurements. The reduction process of CoO_x is $Co^{3+} \rightarrow Co^{2+} \rightarrow Co^0$, while that of MnO_x is $Mn^{4+} \rightarrow Mn^{3+} \rightarrow Mn^{2+}$. However, the reduction temperature of CoO_x is lower [5,45]. Reduction of pure $CoMnO_x$ is primarily divided into two processes: The first stage is a reduction peak centered on 435 and 495 °C, dominated by CoO_x reduction, whereas the second stage is centered on 562 °C and attributable to MnO_x reduction [5]. The reduction peaks of the three samples for the changed catalysts shifted systematically to lower temperatures, showing that this alteration increased the reducibility of the catalysts [28,46,47]. The sulfate-treated sample ($CoMnO_x$-TAA) had the best reduction performance, followed by the phosphorylated material ($CoMnO_x$-AP), and finally the sulphuric acid solution-treated catalyst ($CoMnO_x$-S). $CoMnO_x$-TAA has an excellent redox capacity, which is closely related to an increase in specific surface area, full exposure of active species and increased lattice oxygen mobility (promotes the generation of oxygen vacancies on surfaces). This advantage possessed by $CoMnO_x$-TAA can effectively avoid the Cl_2 formation temperature window (low temperature section) in the depletion reaction [48].

NH_3-TPD profiles of the catalysts illustrated in Fig. 5b-c and Fig. S10 are separated into three sections within above 500 °C, 300–500 °C and 100–300 °C, corresponding to ammonia desorbed from strong, moderate and weak acid sites [18,49–52]. Apparently, only strong acid sites were observed in the TPD curves of pure $CoMnO_x$ and no weak or moderate acid sites were present. For the $CoMnO_x$-S, a desorption peak appeared at 205 °C, indicating that weak acid sites were generated in this catalyst. Furthermore, this further confirms that the acidic sites on the catalyst surface were significantly enhanced in the sulphuric acid solution-treated samples due to the presence of surface sulfate. For $CoMnO_x$-AP and $CoMnO_x$-TAA, the NH_3 desorption peaks showed numerous weak and moderate acid sites, indicating similar acid strengths on the surfaces of both catalysts, but significant differences in the areas of the desorption peaks. We calculated the sum of the number
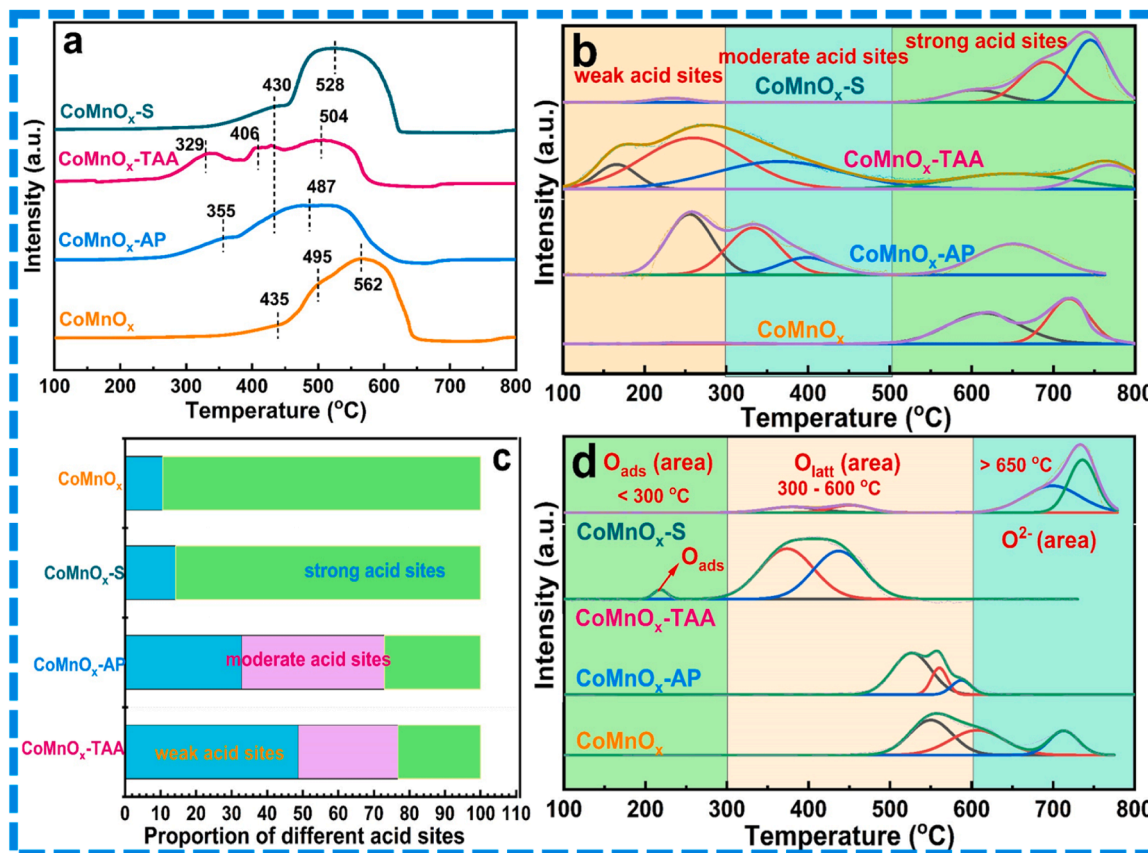

Fig. 5. (a) H_2-TPR, (b and c) NH_3-TPD and (d) O_2-TPD profiles of prepared catalysts.

of weak and moderate acid sites (Table 2). The sum of weak and moderate acid sites follows the trend of $CoMnO_x$-TAA > $CoMnO_x$-AP > $CoMnO_x$-S > $CoMnO_x$. This may be related to the significant increase in the specific surface area of the catalyst after the acid modification treatment. The $CoMnO_x$-TAA sample possesses an excellent surface acidic site, which provides an adsorption center for the o-DCB molecule, and the C-Cl bonds in the o-DCB molecule tend to adsorb on its surface. We hypothesized that the synergistic effect between abundant acidic sites and good redox properties could promote the adsorption and activation of o-DCB on $CoMnO_x$-TAA catalyst.

O_2-TPD was performed to observe the mobility of oxygen species (Fig. 5d). Commonly, there are three principal types of desorbed oxygen species: surface chemical or physically adsorbed oxygen (O_2, O_2^- and O^-) desorbed at 100–300 °C, surface lattice oxygen (O_{latt}) desorbed at 300–600 °C, bulk lattice oxygen (O^{2-}) above 700 °C. Adsorbed oxygen and O_{latt} are essential for the catalytic oxidation of o-DCB [5,52–55]. For both $CoMnO_x$ and $CoMnO_x$-S, the desorption peaks are from both O_{latt} and O^{2-}, while the O_{latt} desorption peak is earlier for the $CoMnO_x$-S material than for $CoMnO_x$. The $CoMnO_x$-AP and $CoMnO_x$-TAA catalysts have abundant O_{latt}, but $CoMnO_x$-TAA has significantly more O_{latt}. More importantly, $CoMnO_x$-TAA showed adsorbed oxygen desorption peaks at lower temperatures, which further enhanced the catalytic oxidation activity of the catalysts. In conclusion, after acid modification, the catalyst oxygen species migration capacity was significantly enhanced in favor of accelerated o-DCB oxidation.

3.6. DFT-calculation study

The Gibbs free energy (ΔG) of the Cl removal process of o-DCB over $Co_2MnO_{4.5}$ catalyst was calculated by density functional theory (DFT). The influence of Cl removal process on the catalytic combustion of o-DCB and the reaction mechanism are revealed. Detailed theoretical calculations are given in the supporting information.

To facilitate the theoretical calculations, the o-DCB molecular model was optimized as shown in Fig. 6 and Fig. S11. Co as the main active site adsorbs the o-DCB molecule firmly on its surface. As the reaction proceeds, first one Cl^- is removed, and then another Cl^- is removed. The removed Cl^- is adsorbed on the Mn site, so the Mn site protects the Co site from Cl toxicity to some extent. In the calculations, the negative value of the free energy indicates exothermic. Step 1: o-DCB → CB+Cl^-, $\Delta G = -0.84$ eV, and step 2: CB → B+Cl^- ($\Delta G = -0.61$ eV). Both steps are exothermic and have high total reaction energy. The benzene ring of B remained intact after removal of the two Cl on o-DCB, suggesting that ring opening and activation of the benzene ring are critical steps in the degradation of o-DCB. The results indicate that o-DCB can spontaneously remove Cl^- at $Co_2MnO_{4.5}$ catalyst, the removed Cl^- adsorbed at the Mn site, and the formation of B oxidized is the key step to degrade o-DCB.

3.7. Catalytic performance analysis

Fig. 7 illustrates the deep catalytic oxidation activity of $CoMnO_x$ and modified catalysts for o-DCB. More specifically, both $CoMnO_x$ and $CoMnO_x$-S exhibited poor catalytic activities for the catalytic decomposition of o-DCB, while significantly increased activities were observed for the $CoMnO_x$-AP and $CoMnO_x$-TAA catalysts, especially $CoMnO_x$-TAA (Fig. 7a). Table 3 also summarizes the 10%, 50% and 90% o-DCB conversion temperatures of the prepared materials (T_{10}, T_{50} and T_{90}). According to the obtained values of T_{90}, the catalyst oxidation activity increased in the order $CoMnO_x$ < $CoMnO_x$-S < $CoMnO_x$-AP < $CoMnO_x$-TAA. Overall, the catalytic oxidation activity of the modified catalyst was significantly increased and the conversion curve moved to lower temperatures, suggesting that the acid modification of pure $CoMnO_x$ facilitated the oxidative decomposition of o-DCB.

Investigating the effect of H_2O on prepared samples has a grand significance (Fig. 7b). After 300 min, water vapor (5 vol%) was

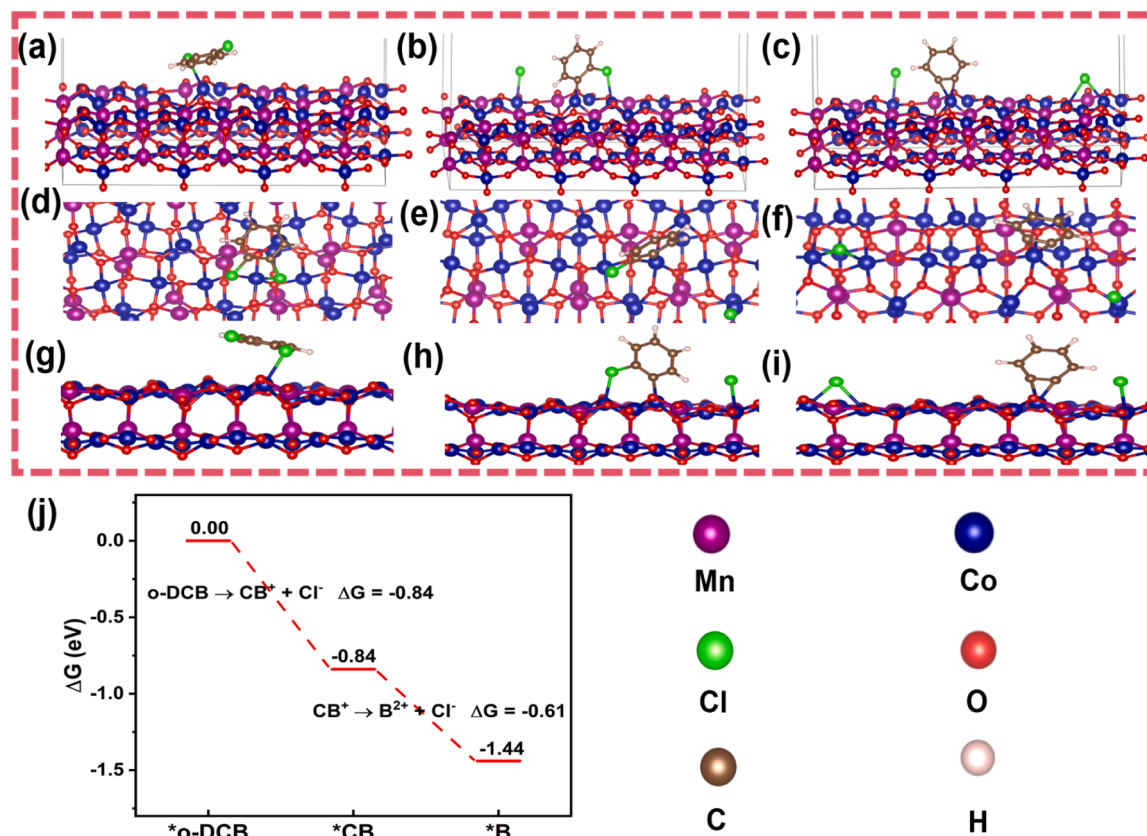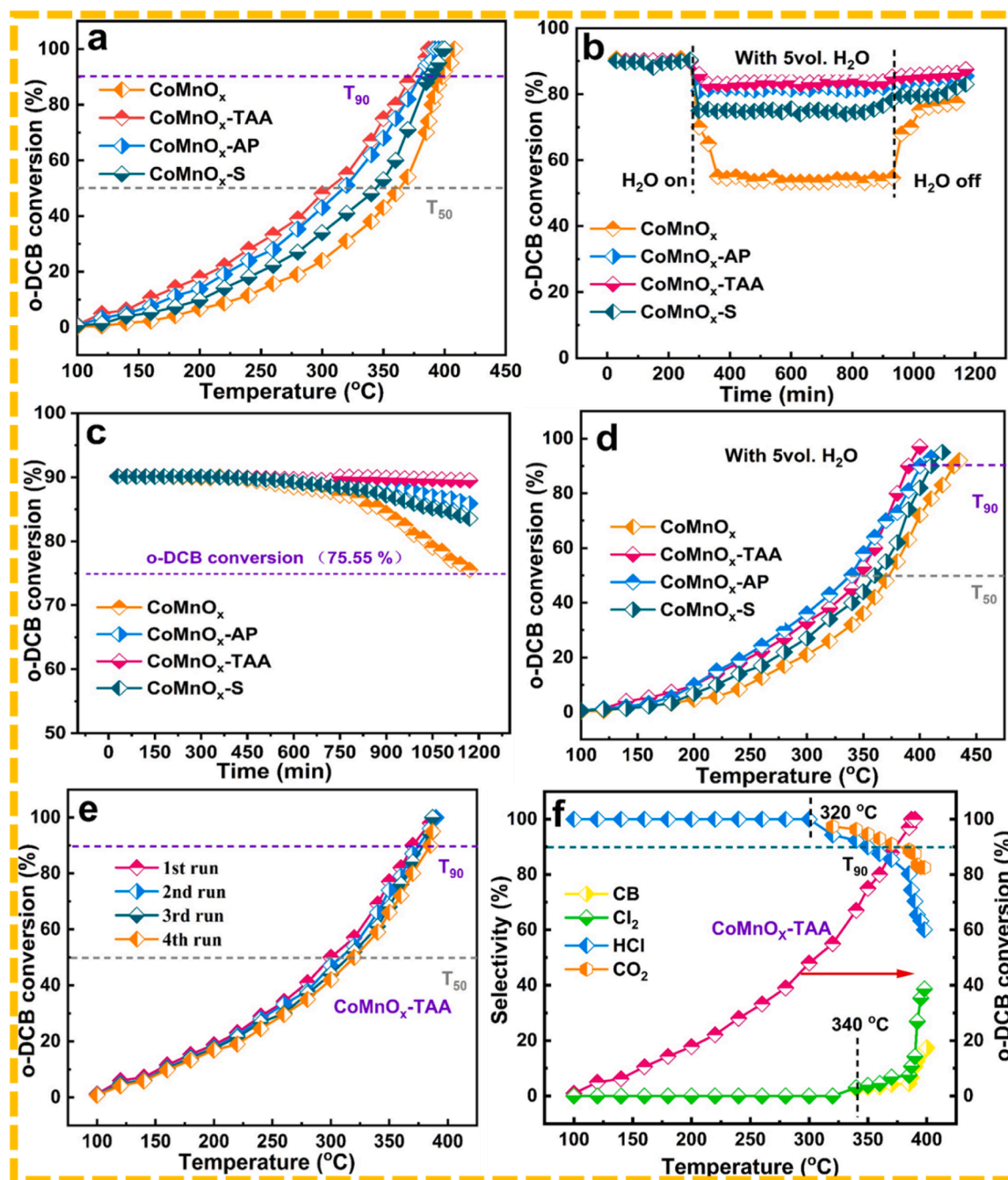**Fig. 6.** (a-i) The optimized model for o-DCB and o-DCB adsorbed on $Co_2MnO_{4.5}$, (j) gibbs free energy value of dechlorination process.

Fig. 7. (a) Catalytic activity, (b) anti-H$_2$O ability, (c) thermal stability, (d) catalytic activity with 5 vol% H$_2$O conditions, (e) reusability and (f) selectivity of synthesized catalysts.

Table 3
Catalytic performance of synthesized CoMnO$_x$ and modified materials for o-DCB degradation.

Catalysts	E$_a$ (kJ mol^{-1})	T$_{10}$ (°C)	T$_{50}$ (°C)	T$_{90}$ (°C)	TOFs at 320 °C (μmol (m^{-1} s^{-1}))
CoMnO$_x$	60.58	210	360	402	0.84
CoMnO$_x$-AP	46.64	178	310	381	1.79
CoMnO$_x$-TAA	36.91	164	295	373	2.06
CoMnO$_x$-S	52.44	205	345	387	1.47

introduced into the reactant flow, reducing the catalytic activity of the CoMnO$_x$ material from 90% to 55%, indicating that the H$_2$O exhibited inhibition due to the competitive adsorption of H$_2$O molecules and o-DCB at the active site. The surface of the catalyst after acid treatment may contain some hydrophobic functional groups, which hinder the adsorption of water molecules on the active sites. After 900 min, the water vapor was turned off, and the conversion of o-DCB began to recover gradually. Remarkably, the presence of H$_2$O decreased the activity of four catalysts for o-DCB oxidation, with the degree of inhibition in the following order: CoMnO$_x$-TAA < CoMnO$_x$-AP < CoMnO$_x$-S < CoMnO$_x$. On the other hand, the acid treatment greatly increased the specific surface area of the catalyst and the number of active sites on the catalyst surface. Therefore, even though competitive adsorption of H$_2$O molecules and o-DCB occurred on the active sites, the effect on the

catalyst activity is not significant. In addition, the acid-modified treatment resulted in the formation of abundant acidic sites on the catalyst surface, which combined with the hydroxyl groups inside the H_2O molecule to favor the formation and desorption of HCl. For the modified catalysts, it leads to the generation of more HCl during o-DCB oxidation during the water resistance test. The adsorption of water molecules of the catalyst can be inhibited, thus maintaining the water resistance of o-DCB oxidation. Notably, CoMnO$_x$-TAA not only has outstanding catalytic stability and activity but also excellent water resistance.

Fig. 7c demonstrates the thermal stability performance of CoMnO$_x$ and modified catalysts tested for resistance to poisoning. All prepared materials were subjected to 1200 min thermal stability performance tests for the oxidative decomposition of o-DCB. After 600 min, pristine CoMnO$_x$ started to deactivate and the o-DCB conversion decreased from 90% to 75.5% at 20 h. After 900 min of catalytic oxidation, there was a slight decrease in the stability of CoMnO$_x$-AP and CoMnO$_x$-S, to 85.88% and 83.55%, respectively. The modified catalysts both showed better thermal stability properties. Very encouragingly, the o-DCB conversion of CoMnO$_x$-TAA could be consistently stabilized at a very satisfactory state, with almost negligible decay of the initial T$_{90}$ activity.

Fig. 7d further demonstrates the effect of H_2O content on the conversion rate of o-DCB. Clearly, the degree of inhibition was more pronounced for water at low temperatures. The T$_{90}$ and T$_{50}$ of all prepared samples increased to varying degrees. In the presence of 5 vol% H_2O, the conversion of o-DCB on CoMnO$_x$ and modified catalysts before 320 °C was significantly lower compared to the previous test results (Fig. 7a). Especially for CoMnO$_x$-TAA, the decrease in activity at the high-temperature stage was almost negligible, showing excellent water resistance at high temperatures. In conclusion, the TAA-modified CoMnO$_x$ products has a high practical application value.

In addition, we explored the reusability of CoMnO$_x$-TAA with better catalytic activity (Fig. 7e). Through multiple tests, the T$_{90}$ of CoMnO$_x$-TAA for the catalytic decomposition of o-DCB was consistently maintained in the range of 373–381 °C. The above results suggest that this sample exhibits excellent reusability performance as there may be an equilibrium state between the adsorption and desorption of Cl.

Furthermore, we investigate the product selectivity of the oxidative decomposition o-DCB of CoMnO$_x$-TAA materials (Fig. 7f). We observed that the dominant products of the catalytic oxidation stage are HCl and CO_2, especially after 320 °C. In general, HCl is less toxic and more convenient to handle than chlorobenzene (CB) and Cl_2. With increasing reaction temperatures (after 340 °C), a small amount of CB and Cl_2 are generated due to the further oxidation of HCl at high temperatures. Other organic intermediates exceeding the detection limit of FID were not found, which showed that CoMnO$_x$-TAA not only significantly enhanced the conversion rate of o-DCB but also increased the mineralization rate of organic intermediates. In short, CoMnO$_x$-TAA accelerates the dissociation of the C-Cl bond (extraction of chlorine) and promotes the formation of HCl, which makes the catalyst exhibits high selectivity for HCl, but low selectivity for Cl_2.

Generally, the oxidative decomposition of the catalyst to o-DCB goes through four steps: o-DCB adsorption, Cl dissociation, C-C and C-Cl bond cleavage and further deep oxidation (into H_2O and CO_2). Compared with other modified materials, we found that CoMnO$_x$-TAA material has stronger Cl dissociation ability and C-H and C-C bond cleavage ability, so its activity is more prominent in the o-DCB catalytic process, which is ascribed to its outstanding O_{latt} content, O_{ads} mobility, large specific surface area and rich reducible Co^{3+} and Mn^{4+} species. Based on the above analysis, CoMnO$_x$-TAA material has excellent Cl desorption ability, effectively inhibits the yield of by-products, and has better product selectivity for the destruction of o-DCB.

Table 4 compares the oxidative decomposition performance of o-DCB on CoMnO$_x$-TAA material with previous related studies. CoMnO$_x$-TAA samples exhibited superior low-temperature catalytic oxidation than comparable CoMn catalysts, and their stability and water resistance were significantly improved, indicating that the acid modification of the

Table 4
Comparison of catalytic materials for o-DCB oxidation decomposition reported in the literature with this study.

Catalysts	T$_{50}$ (°C)	T$_{90}$ (°C)	Concentration (ppm)	GHSV mL (g·h)$^{-1}$	Refs.
CoMn600 @ 0.25Ti	352	416	1000	30000	[5]
MnO$_x$	328	< 450	1000	30000	[33]
Co3Mn1	337	378	1000	30000	[33]
15CM/TS-1.5	310	364	500	15000	[46]
CoCuO$_x$ @CeO$_2$	340	395	1000	15000	[18]
Pt/H-BETA	352	425	500	15000	[51]
Pt/CeO$_2$	334	431	1000	60000	[48]
CeMn/TiO$_2$-SiO$_2$	310	378	1000	30000	[5]
C-Mn	328	410	-	-	[37]
CoMnO$_x$-AP	310	381	1000	15000	This work
CoMnO$_x$-TAA	295	373	1000	15000	This work

catalyst was very successful. In addition, CoMnO$_x$-TAA also exhibited excellent selectivity, with high selectivity for HCl, but low selectivity for Cl_2. The above results indicate that the synthesized CoMnO$_x$-TAA is an eco-friendly catalyst that is not harmful to the environment.

In this paper, we have investigated the catalytic decomposition performance of the samples using kinetic calculations (Table S2). According to related reports, the oxidative decomposition of o-DCB in the presence of sufficient oxygen follows a first-order kinetic mechanism [5, 18]. The calculation follows the following equation: $r = A \cdot exp\ (-E_a/RT)\ C_{o\text{-}DCB}$, where the calculation process for the apparent activation energy (E_a) is reflected in the supporting information. The E_a value for CoMnO$_x$-TAA was found to be 36.91 kJ mol^{-1}, which was lower than those of CoMnO$_x$-AP (46.64 kJ mol^{-1}), CoMnO$_x$-S (52.44 kJ mol^{-1}) and CoMnO$_x$ (60.58 kJ mol^{-1}) (see Table 3 and Fig. 8a). The excellent catalytic activity of CoMnO$_x$-TAA is associated with its smaller E_a, which means that the lower the energy barriers (the C-H bond dissociation energy) during the catalytic degradation of o-DCB, the more favorable the elimination of o-DCB. Additionally, to investigate the intrinsic activity (TOF) of the synthesized materials, we calculated the TOF at 300 °C (Table 3). TOF value calculations are displayed in the supporting information. The TOF$_{Co}$ for CoMnO$_x$, CoMnO$_x$-AP, CoMnO$_x$-TAA and CoMnO$_x$-S catalysts are 0.84, 1.79, 2.06 and 1.47 μmol (m^{-1} s^{-1}), respectively, suggesting that the highest intrinsic activity of CoMnO$_x$-TAA catalyst.

3.8. Pivotal factors affecting o-DCB destruction

We calculated the reaction rate constants (r) of o-DCB oxidative decomposition over synthesized catalysts at 200 °C in Fig. 8b, which follows the order of CoMnO$_x$-TAA (3.29 μmol(m^{-2} s^{-1})) > CoMnO$_x$-AP (3.06 μmol(m^{-2} s^{-1})) > CoMnO$_x$-S (2.71 μmol(m^{-2} s^{-1})) > CoMnO$_x$ (2.58 μmol(m^{-2} s^{-1})), suggesting that the CoMnO$_x$-TAA owns superior catalytic activity and is a promising catalyst for o-DCB destruction. In addition, r and TOF also corresponded well. From E_a and T$_{90}$ versus O_{latt} (Fig. 8c), catalysts with high levels of O_{latt} had lower E_a and T$_{90}$, which reinforces that the role of O_{latt} in o-DCB catalytic combustion cannot be overlooked. Fig. 8d demonstrates that T$_{50}$ and T$_{90}$ decrease with the increase in Co^{3+} and Mn^{4+} concentration, suggesting that Co^{3+} and Mn^{4+} are crucial for o-DCB oxidation. Fig. 8e presents the relationship between r and E_a versus acid sites. Samples with more abundant surface moderate and weak acid sites have larger r and smaller E_a, indicating that acid sites are particularly important for the combustion destruction of o-DCB over the synthetic catalysts at low temperatures. Fig. 8f depicts the relationship between O_{latt} and r, r becomes larger with increasing O content, indicating that O_{latt} facilitates the catalytic oxidation of o-DCB and can accelerate the decomposition of o-DCB.
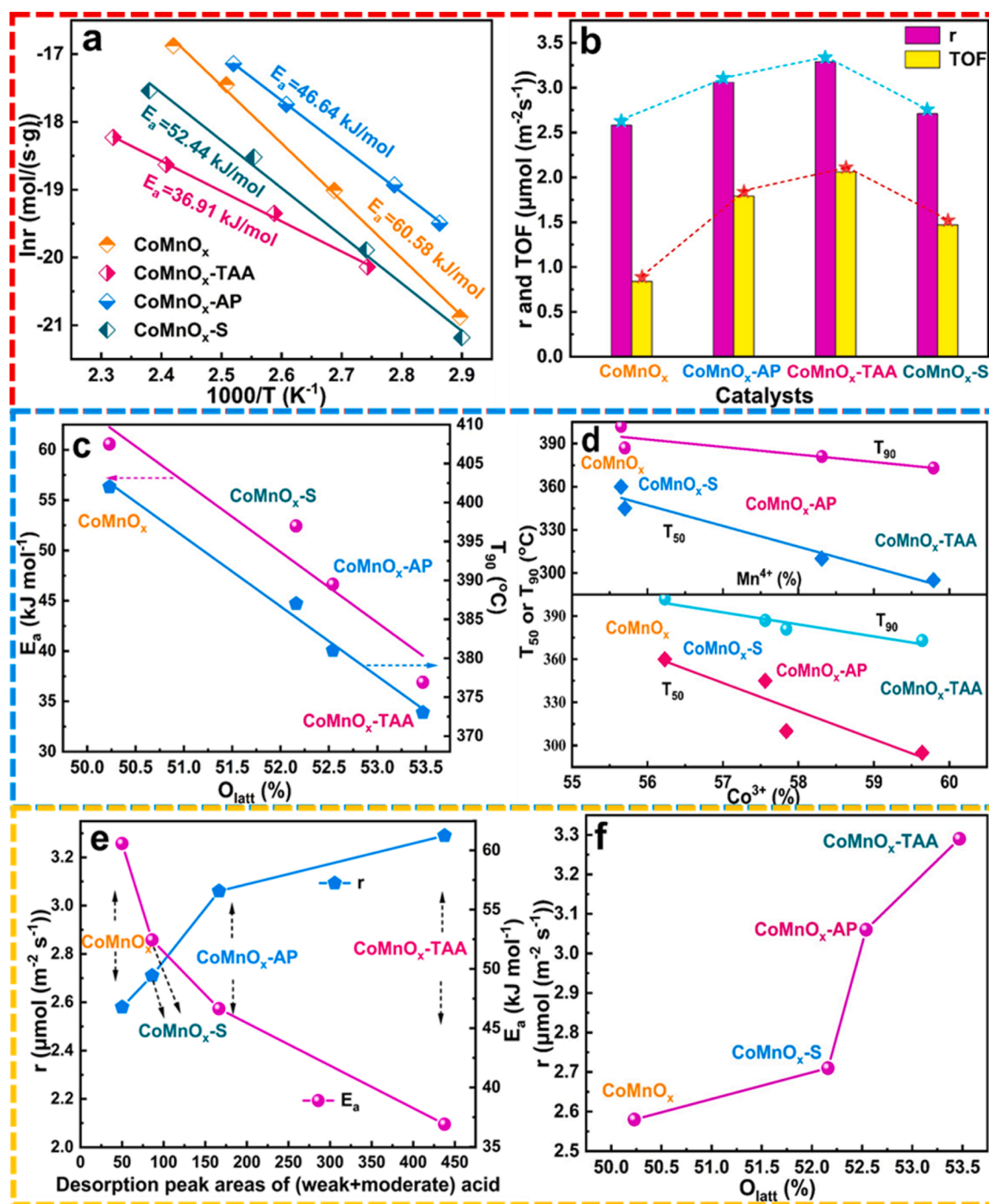
Fig. 8. (a) Apparent activation energy, (b) reaction rate and intrinsic activity, (c) apparent activation energy and catalytic activity versus lattice oxygen, (d) catalytic activity and active metal species, (e) reaction rate and apparent activation energy versus acid site, and (f) reaction rate versus lattice oxygen.

3.9. TPSR study

The TPSR results of o-DCB over CoMnO$_x$-TAA catalysts are exhibited in Fig. 9 and Fig. S12, where the destruction process of o-DCB and the change of products can be clearly observed. When o-DCB was catalytically combusted, the main products of the reaction were HCl and CO$_2$ (Due to the oxidative dissociation of the C-Cl bond Cl atoms are generated, and the generated Cl atoms further combine with protons on the catalyst at low temperatures to generate HCl). In addition, trace amounts of CB and Cl$_2$ were detected, which was in high agreement with the results of the by-product selectivity analysis on the FID detection equipment. Probably because of the high oxidizing power of the catalyst,

there was no obvious signal of CO detection. The CO signal weakness may be due to the involvement of surface lattice oxygen, where CO is quickly oxidized to CO$_2$ (2CO + O$_2$ = 2CO$_2$). It should be noted that due to the low sensitivity of FID, no CO signal was detected in the analytical detection.

3.10. The possible reaction mechanism

Fig. 10 depicts in situ FTIR spectra of o-DCB adsorption and oxidation reaction over CoMnO$_x$-TAA material. In situ FTIR of o-DCB adsorption at 150 °C at different times is presented in Fig. 10a. Clearly, the typical peak intensities of o-DCB began to gradually increase as
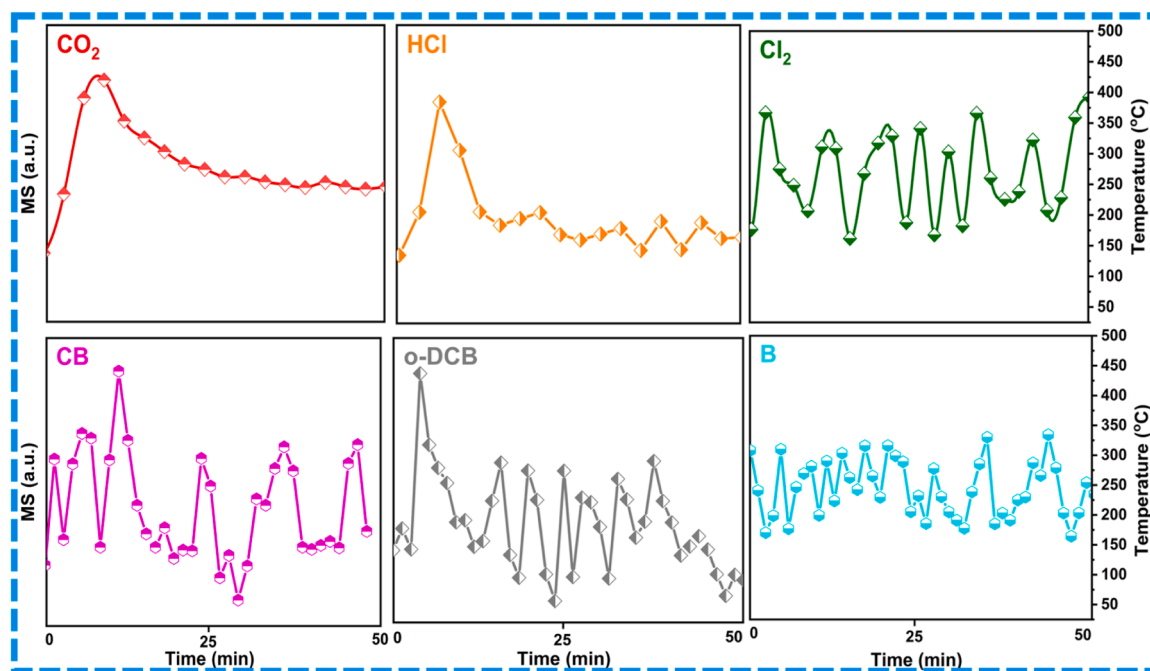
Fig. 9. TPSR studies of o-DCB catalytic destruction for B ($m/z = 78$), CB ($m/z = 112$), o-DCB ($m/z = 148$), CO_2 ($m/z = 44$), HCl ($m/z = 36$), Cl_2 ($m/z = 70$).

observed from the 1–24 min curves of adsorption, and after 20 min, the intensities of these characteristic peaks were unchanging, indicating that the o-DCB reached saturation in 20 min of adsorption (Fig. S13). The vibration of the C-Cl bond in chlorinated phenols forms an inconspicuous band at 1014 cm^{-1} [18]. The C-H in-plane bending vibration is responsible for the band at 1236 cm^{-1} [2,47]. The stretching vibrations of the aromatic ring are thought to be responsible for the spectral bands with wave numbers of 1485 and 1388 cm^{-1} [41,49]. Additionally, the weak band at 1608 cm^{-1} is attributed to C=C [20,49,56]. Fig. 10b record in situ FTIR spectra of o-DCB adsorbed at various temperatures exposed for 25 min. When the adsorption temperature was gradually increased to 200 and 250 °C, the weak bands at 1433, 1556, and 1652 cm^{-1} vanished. Moreover, the bands of 1274, 1164, 1118 and 1018 cm^{-1} are caused by the formation of weak C-O bonds. Surprisingly, new IR bands have emerged as a result of rising temperatures, and the intensity of these bands has progressively intensified. Additionally, the sharp band at 1487 cm^{-1} is associated with a carbonate bidentate [50,57]. A weak band at 1683 cm^{-1} corresponds to surface enolic species [52,56]. The indistinct band at 1597 cm^{-1} is ascribed to COOH-from bidentate formate [51,57,58].

Fig. 10c-d demonstrates the in situ FTIR spectra of the CoMnO$_x$-TAA catalyst under different conditions. The spectra of the oxidation reaction at 150 °C at different times (Fig. 10c) show several similarities to the adsorption spectra (Fig. 10a). After 17 min, the intensity of the oxidation reaction spectrum remained nearly constant, and no new reaction peaks were generated. The results in Fig. 10c shows that the CoMnO$_x$-TAA catalyst had little effect in catalyzing the oxidation reaction at 150 °C, with only a very small amount of o-DCB being desorbed. The above results also further indicate the weak adsorption of oxygen by the sample when it is exposed to O$_2$ at 150 °C. As the temperature increased, we found a significant change in the oxidation profile at 200 °C in Fig. 10d, which indicates that o-DCB was barely oxidized over the CoMnO$_x$-TAA catalyst when the temperature was below 200 °C (consistent with Fig. 7a). At temperatures up to 250 °C, some new oxidation spectral bands appeared and the intensity of these bands increased and then decreased as the temperature continued to rise, which may be ascribed to the formation of intermediates, indicating the gradual oxidation of o-DCB.

As the temperature rises to 300 °C or higher, the band associated with the oxygen-containing intermediates becomes weaker, indicating a further involvement of surface oxygen in the oxidation reaction. Obviously, after the oxidation temperature reached 300 °C, the intensity of the original band at 1022 cm^{-1} became weaker and the energy band at 1022 cm^{-1} disappeared when the temperature was increased to 350 °C. This indicates that the o-DCB was decomposed at this point and the C-Cl bond was broken through the extraction of Cl ions. The strong band at 1272 cm^{-1} is triggered by CH$_2$- or CH- vibrations, which means that o-DCB is adsorbed and activated [4]. In comparison to the adsorption spectra of the material in the (o-DCB + N$_2$) flow, the introduction of O$_2$ significantly enhanced the oxidation spectra of o-DCB (at 1073, 1126, 1161 and 1485 cm^{-1}). The spectral bands at 1551 cm^{-1} weaken and fade after 350 °C, possibly associated with the asymmetric stretching of carboxylate species, which implies the destruction of the o-DCB. The weak band at 1602 cm^{-1} is caused by vibrations of hydroxyl groups in the water and attributed to the oxidation of adsorbed species in the catalyst [4]. Fig. 10f-h show the spectra of CoMnO$_x$-TAA oxidized o-DCB at different temperatures under different atmospheres. In conclusion, the analysis of the in situ FTIR results indicates that the oxidative decomposition of o-DCB starts with the decomposition of C-Cl to formate and carboxylate, followed by oxidation to CO$_2$ and H$_2$O. Possible reaction pathways: o-DCB→ VC (vinyl chloride)→ alcohol→ aldehyde→ acetic acid→ CO$_x$ [20,47]. Fig. S14 shows the reaction process of o-DCB adsorption and oxidation over CoMnO$_x$ catalyst.

Based on catalytic performance tests and in situ FTIR, we propose a feasible reaction route and reaction mechanism for o-DCB oxidative degradation over CoMnO$_x$-TAA catalyst (Scheme 2). In this work, weak and medium acid sites, active species and lattice oxygen play a decisive role in the decomposition and destruction of o-DCB. Consequently, consideration of the oxidative decomposition of o-DCB over CoMnO$_x$-TAA catalysts ought to comply with the Mars-van-Krevelen (MvK) mechanism. In step 1, the active sites on the catalyst surface adsorb o-DCB molecules and the C-Cl bond is cleaved by the active species allowing the dissociated chlorine species to emerge. In step 2, activation and dissociation of o-DCB with surface lattice oxygen and nucleophilic substitution of C-Cl by lattice oxygen allows rapid adsorption of Cl$^-$ onto the active components Co^{3+} and Mn^{4+}, thus the chlorinated phenolate species is then converted to a non-chlorinated phenolate species. In step 3, the dissociated o-DCB is oxidized to primary intermediates (phenols)
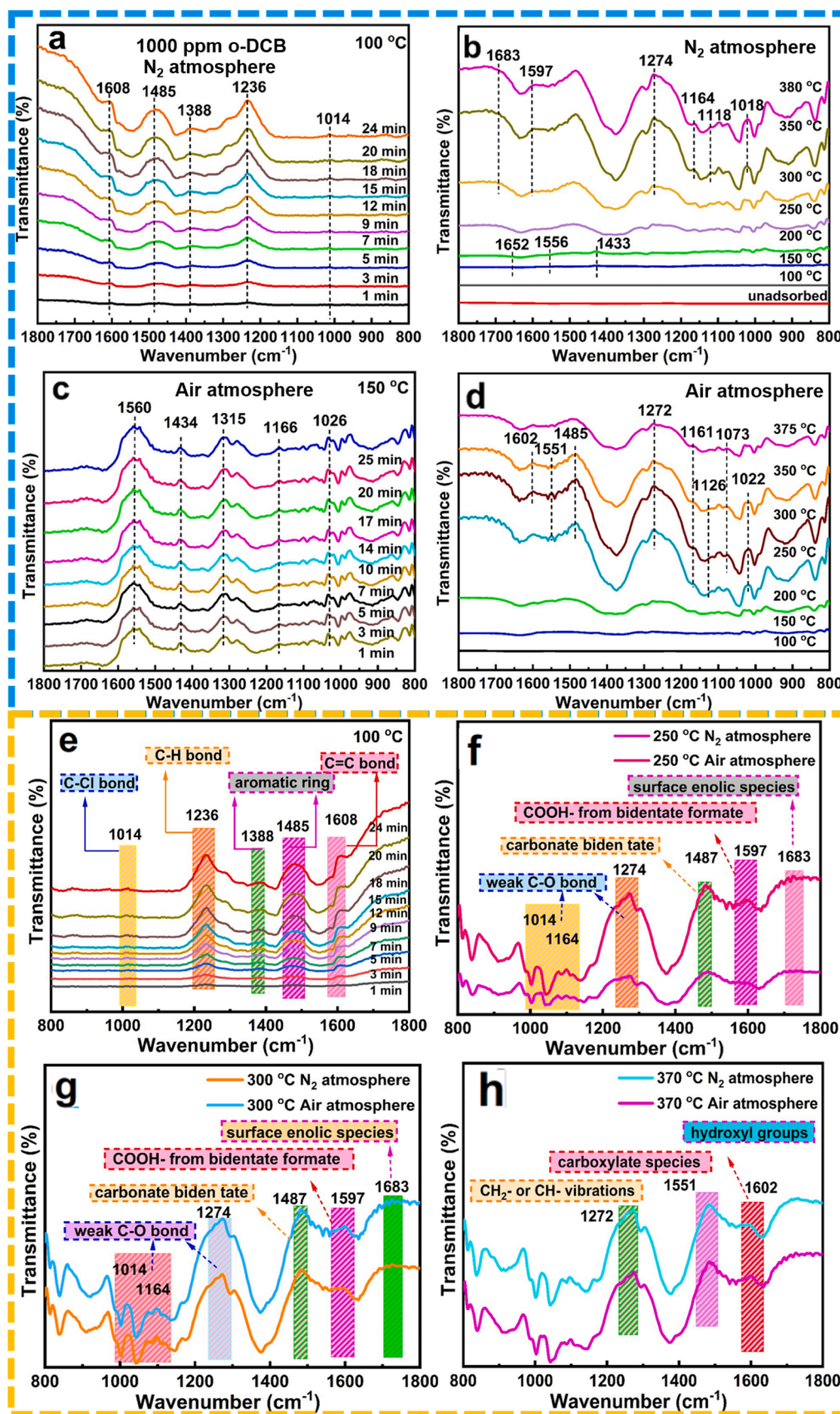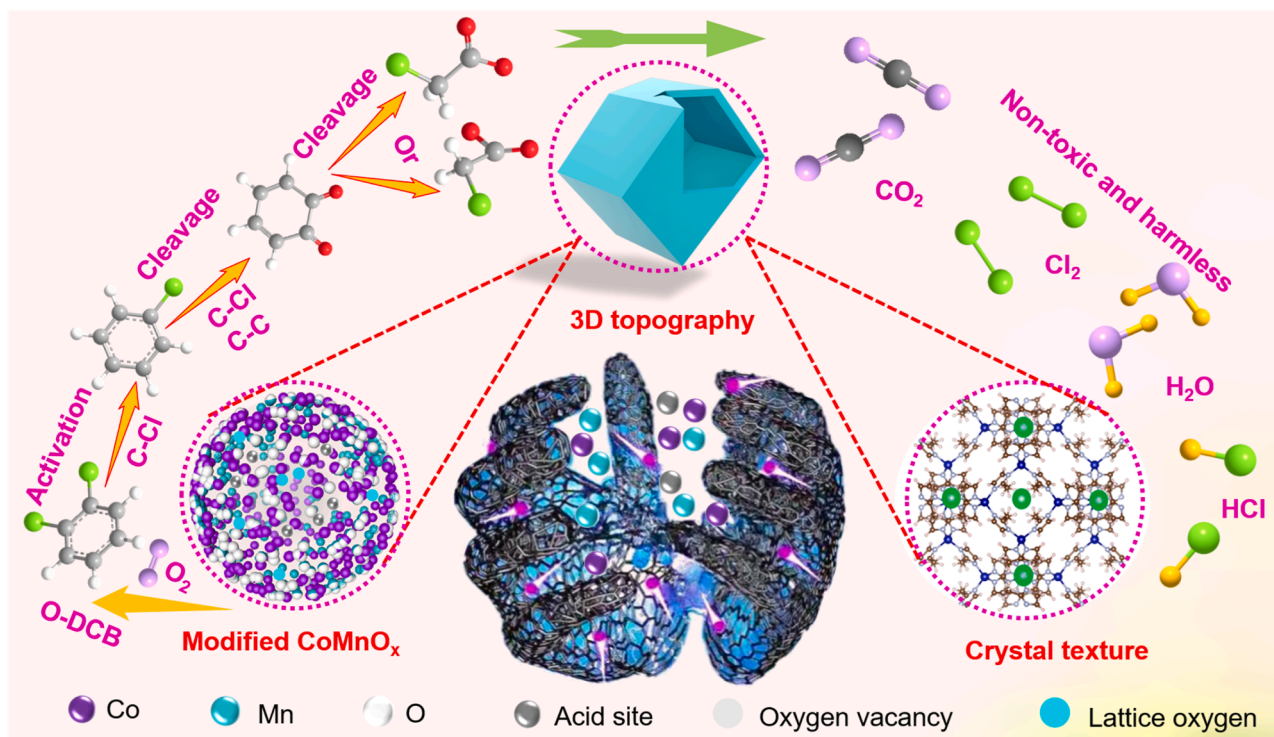
Fig. 10. (a, b and e) In-situ FTIR spectra for adsorption exposure to 1000 ppm o-DCB in N_2 and (c and d) oxidation o-DCB at air and (f-h) under different atmospheres at different temperatureon the CoMnO$_x$-TAA.

Scheme 2. Proposed o-DCB destruction mechanism over CoMnO$_x$ catalysts.

via lattice oxygen, the phenols are then continued to oxidation to form quinone sulfonic acid intermediates, and the deposited Cl$^-$ are eventually removed as a combination with H (from H$_2$O) to form Cl$_2$ or HCl and carboxylate intermediates through to CO$_2$. In the mechanism proposed here, weak and moderate acid sites and lattice oxygen are indispensable for the catalytic degradation of o-DCB.

4. Conclusions

Tuning the surface acidity and redox properties of CoMnO$_x$ nanostructures is a prospective approach to developing efficient catalysts for the catalytic decomposition of o-DCB. EPR confirmed that the acid modification produced abundant oxygen vacancies on the catalyst surface, particularly in CoMnO$_x$-TAA. Through O$_2$-TPD and XPS, we found that the amount of Co^{3+} and Mn^{4+} species with a strong oxidation ability increased by phosphorization and sulfurization. After acid modification, oxygen atoms combine with metal atoms on the surface to form many metal vacancies, and the resulting metal defects contribute to the exposure of more active sites. Effectively regulates the adsorption capacity of reactants and accelerates the kinetics of surface reactions. Acid modification promotes the migration of active oxygen, which is conducive to the further oxidation of intermediates in the process of o-DCB catalytic degradation as well as contributing to the anti-coking properties. TPSR indicates that the oxidative dissociation of C-Cl bonds generates Cl atoms that further combine with protons on the catalyst at low temperatures to generate HCl, with the main reaction products being CO$_2$ and HCl. Furthermore, the formation of acid-rich sites driven would facilitate o-DCB dissociation, and the generated weak and moderate acidic sites improve HCl selectivity. DFT calculations show that o-DCB can spontaneously remove Cl$^-$ in catalytic combustion, and the formation of B oxidized is the key step to degrade o-DCB. CoMnO$_x$-TAA and CoMnO$_x$-AP showed considerable activity and excellent stability towards o-DCB combustion degradation. Comparing the water resistance of the prepared catalysts, the reversibility of H$_2$O was found for CoMnO$_x$-TAA and the inhibition became weaker at higher reaction temperatures. More importantly, several pivotal factors affecting the elimination of o-DCB have been meticulously investigated. The above studies provide a viable strategy for the industrial catalytic decomposition of o-DCB through the modulation of surface acidity.

CRediT authorship contribution statement

Shixing Wu: Investigation, Methodology, Formal analysis, Writing – original draft. **Shilin Wu:** Computational modeling, Data curation. **Fang Dong:** Conceptualization, Writing – review & editing. **Yuntai Xi:** Investigation, Methodology. **Peng Wang:** Computational modeling, DFT calculation. **Yinghao Chu:** Conceptualization, Resources. **Zhicheng Tang:** Supervision, Funding acquisition, Writing – review & editing. **Jiyi Zhang:** Supervision, Writing – review & editing.

Declaration of Competing Interest

The authors declare that they have no known competing financial interests or personal relationships that could have appeared to influence the work reported in this paper.

Data Availability

The authors do not have permission to share data.

Acknowledgments

Appendix A. Supporting information

Supplementary data associated with this article can be found in the online version at doi:10.1016/j.apcatb.2023.123390.

References

[1] H. Zhang, X. Gao, B. Gong, B. Shao, C. Tu, J. Pan, Y. Wang, Q. Dai, Y. Guo, X. Wang, Catalytic combustion of CVOCs over MoO_x/CeO_2 catalysts, Appl. Catal. B: Environ. 310 (2022), 121240.

[2] X. Lv, M. Jiang, J. Chen, D. Yan, H. Jia, Unveiling the lead resistance mechanism and interface regulation strategy of Ru-based catalyst during chlorinated VOCs oxidation, Appl. Catal. B: Environ. 315 (2022), 121592.

[3] X. Yu, L. Dai, J. Deng, Y. Liu, L. Jing, X. Zhang, R. Gao, Z. Hou, L. Wei, H. Dai, An isotopic strategy to investigate the role of water vapor in the oxidation of 1, 2-dichloroethane over the Ru/WO_3 or Ru/TiO_2 catalyst, Appl. Catal. B: Environ. 305 (2022), 121037.

[4] Y. Huang, M. Tian, Z. Jiang, M. Ma, C. Chen, H. Xu, J. Zhang, R. Albilali, C. He, Inserting Cr_2O_3 dramatically promotes RuO_2/TiO_2 catalyst for low-temperature 1, 2-dichloroethane deep destruction: Catalytic performance and synergy mechanism, Appl. Catal. B: Environ. 304 (2022), 121002.

[5] H. Zhao, W. Han, Z. Tang, Tailored design of high-stability $CoMn_{1.5}O_x@TiO_2$ double-wall nanocages derived from Prussian blue analogue for catalytic combustion of o-dichlorobenzene, Appl. Catal. B: Environ. 276 (2020), 119133.

[6] J. Bae, D. Shin, H. Jeong, C. Choe, Y. Choi, J.W. Han, H. Lee, Facet-dependent Mn doping on shaped Co_3O_4 crystals for catalytic oxidation, ACS Catal. 11 (2021) 11066–11074.

[7] P. Yang, X. Xue, Z. Meng, R. Zhou, Enhanced catalytic activity and stability of Ce doping on Cr supported HZSM-5 catalysts for deep oxidation of chlorinated volatile organic compounds, Chem. Eng. J. 234 (2013) 203–210.

[8] W. Deng, Q. Tang, S. Huang, L. Zhang, Z. Jia, L. Guo, Low temperature catalytic combustion of chlorobenzene over cobalt based mixed oxides derived from layered double hydroxides, Appl. Catal. B: Environ. 278 (2020), 119336.

[9] N. Jiang, Y. Zhao, C. Qiu, K. Shang, N. Lu, J. Li, Y. Wu, Y. Zhang, Enhanced catalytic performance of $CoO-CeO_2$ for synergetic degradation of toluene in multistage sliding plasma system through response surface methodology (RSM), Appl. Catal. B: Environ. 259 (2019), 118061.

[10] F. Lin, Z. Zhang, N. Li, B. Yan, C. He, Z. Hao, G. Chen, How to achieve complete elimination of Cl-VOCs: A critical review on byproducts formation and inhibition strategies during catalytic oxidation, Chem. Eng. J. 404 (2021), 126534.

[11] H. Li, H. Song, L. Chen, C. Xia, Designed $SO_4^{2-}/Fe_2O_3-SiO_2$ solid acids for polyoxymethylene dimethyl ethers synthesis: The acid sites control and reaction pathways, Appl. Catal. B: Environ. 165 (2015) 466–476.

[12] S. Li, H. Wang, W. Li, X. Wu, W. Tang, Y. Chen, Effect of Cu substitution on promoted benzene oxidation over porous CuCo-based catalysts derived from layered double hydroxide with resistance of water vapor, Appl. Catal. B: Environ. 166–167 (2015) 260–269.

[13] X. Liu, L. Chen, T. Zhu, R. Ning, Catalytic oxidation of chlorobenzene over noble metals (Pd, Pt, Ru, Rh) and the distributions of polychlorinated by-products, J. Hazard. Mater. 363 (2019) 90–98.

[14] Q. Dai, S. Bai, X. Wang, G. Lu, Facile synthesis of HZSM-5 with controlled crystal morphology and size as efficient catalysts for chlorinated hydrocarbons oxidation and xylene isomerization, J. Porous Mater. 21 (2014) 1041–1049.

[15] N. Blanch-Raga, A.E. Palomares, J. Martínez-Triguero, S. Valencia, Cu and Co modified beta zeolite catalysts for the trichloroethylene oxidation, Appl. Catal. B: Environ. 187 (2016) 90–97.

[16] Y. Su, K. Fu, Y. Zheng, N. Ji, C. Song, D. Ma, X. Lu, R. Han, Q. Liu, Catalytic oxidation of dichloromethane over Pt-Co/HZSM-5 catalyst: Synergistic effect of single-atom Pt, Co_3O_4, and HZSM-5, Appl. Catal. B: Environ. 288 (2021), 119980.

[17] X. Du, F. Dong, Z. Tang, J. Zhang, Precise design and synthesis of $Pd/InO_x@CoO_x$ core-shell nanofibers for the highly efficient catalytic combustion of toluene, Nanoscale 12 (2020) 12133–12145.

[18] S. Wu, H. Zhao, Y. Xi, Z. Tang, J. Zhang, Core-shell $CoCuO_x@MO_x$ (M=Nb, Ti and Ce) catalysts with outstanding durability and resistance to H_2O for the catalytic combustion of o-dichlorobenzene, Sci. Total Environ. 860 (2023) 160472.

[19] H. Metiu, S. Chrétien, Z. Hu, B. Li, X. Sun, Chemistry of lewis Acid-base pairs on oxide surfaces, J. Phys. Chem. C. 116 (2012) 10439–10450.

[20] X. Weng, Q. Meng, J. Liu, W. Jiang, S. Pattisson, Z. Wu, Catalytic oxidation of chlorinated organics over lanthanide perovskites: Effects of phosphoric acid etching and water vapor on chlorine desorption behavior, Environ. Sci. Technol. 53 (2019) 884–893.

[21] Z. Yu, S. Li, Q. Wang, A. Zheng, X. Jun, L. Chen, F. Deng, Brønsted/lewis acid synergy in H-ZSM-5 and H-MOR zeolites studied by ^1H and ^{27}Al DQ-MAS solid-state NMR spectroscopy, J. Phys. Chem. C. 115 (2011) 22320–22327.

[22] P. Sun, S. Zhai, J. Chen, J. Yuan, Z. Wu, X. Weng, Development of a multi-active center catalyst in mediating the catalytic destruction of chloroaromatic pollutants: A combined experimental and theoretical study, Appl. Catal. B: Environ. 272 (2020) 119015.

[23] Q. Ying, Y. Liu, N. Wang, Y. Zhang, Z. Wu, The superior performance of dichloromethane oxidation over Ru doped sulfated TiO_2 catalysts: synergistic effects of Ru dispersion and acidity, Appl. Surf. Sci. 515 (2020), 145971.

[24] Q. Dai, K. Shen, W. Deng, Y. Cai, J. Yan, J. Wu, L. Guo, R. Liu, X. Wang, W. Zhan, HCl-tolerant H_xPO_4/RuO_x-CeO_2 catalysts for extremely efficient catalytic elimination of chlorinated VOCs, Environ. Sci. Technol. 55 (2021) 4007–4016.

[25] Q. Ying, Y. Liu, H. Li, Y. Zhang, Z. Wu, A comparative study of the dichloromethane catalytic combustion over ruthenium-based catalysts: Unveiling the roles of acid types in dissociative adsorption and by-products formation, J. Colloid Interf. Sci. 605 (2022) 537–546.

[26] P. Sun, W. Wang, X. Weng, X. Dai, Z. Wu, Alkali potassium induced HCl/CO_2 selectivity enhancement and chlorination reaction inhibition for catalytic oxidation of chloroaromatics, Environ. Sci. Technol. 52 (2018) 6438–6447.

[27] B. Chen, Y. Wen, S. Gao, S. Cao, H. Fu, T. Ding, H. Wang, Z. Wu, Mechanistic insights into the role of acidity to activity and anti-poisoning over Nb based catalysts for CVOCs combustion, Appl. Catal. A: Gen. 636 (2022), 118581.

[28] S. Xu, K.-F. Zhang, Y.-K. Ma, A.-P. Jia, J. Chen, M.-F. Luo, Y. Wang, J.-Q. Lu, Catalytic oxidation of dichloromethane over CrFeO mixed oxides: Improved activity and stability by sulfuric acid treatment, Appl. Catal. A: Gen. 636 (2022), 118573.

[29] H. Liu, J. Yang, Y. Jia, Z. Wang, M. Jiang, K. Shen, H. Zhao, Y. Guo, Y. Guo, L. Wang, S. Dai, W. Zhan, Significant improvement of catalytic performance for chlorinated volatile organic compound oxidation over RuO_x supported on acid-etched Co_3O_4, Environ. Sci. Technol. 55 (2021) 10734–10743.

[30] W.L. Wang, Q. Meng, Y. Xue, X. Weng, P. Sun, Z. Wu, Lanthanide perovskite catalysts for oxidation of chloroaromatics: Secondary pollution and modifications, J. Catal. 366 (2018) 213–222.

[31] X. Qi, T. Lin, K. Gong, X. Wang, D. Lv, F. Yu, Y. An, Z. Tang, L. Zhong, Direct synthesis of higher oxygenates via syngas over zinc oxide modified CoMn-based catalysts, Appl. Catal. A: Gen. 648 (2022), 118925.

[32] W. Han, F. Dong, W. Han, J. Yao, Y. Meng, Z. Tang, A new strategy for designing highly efficient Co_3O_4 catalyst with the molecular space configurations for toluene catalytic combustion, Chem. Eng. J. 435 (2022), 134953.

[33] T. Cai, H. Huang, W. Deng, Q. Dai, W. Liu, X. Wang, Catalytic combustion of 1, 2-dichlorobenzene at low temperature over Mn-modified Co_3O_4 catalysts, Appl. Catal. B: Environ. 166–167 (2015) 393–405.

[34] B. Huang, C. Lei, C. Wei, G. Zeng, Chlorinated volatile organic compounds (Cl-VOCs) in environment-sources, potential human health impacts, and current remediation technologies, Environ. Int. 71 (2014) 118–138.

[35] X. Feng, M. Tian, C. He, L. Li, J.-W. Shi, Y. Yu, J. Cheng, Yolk-shell-like mesoporous $CoCrO_x$ with superior activity and chlorine resistance in dichloromethane destruction, Appl. Catal. B: Environ. 264 (2020), 118493.

[36] X. Fei, S. Cao, W. Ouyang, Y. Wen, H. Wang, Z. Wu, A convenient synthesis of core-shell $Co_3O_4@ZSM-5$ catalysts for the total oxidation of dichloromethane (CH_2Cl_2), Chem. Eng. J. 387 (2020), 124131.

[37] M. Li, J. Mo, X. Gu, Y. Zhou, M. Fan, S. Shen, Y. Chen, Acid modified carrier on catalytic oxidation of dichloromethane over $CeO_2/HZSM-5$ catalysts, J. Rare Earth. 40 (2022) 1564–1572.

[38] Q. Dai, W. Wang, X. Wang, G. Lu, Sandwich-structured $CeO_2@ZSM-5$ hybrid composites for catalytic oxidation of 1, 2-dichloroethane: An integrated solution to coking and chlorine poisoning deactivation, Appl. Catal. B: Environ. 203 (2017) 31–42.

[39] Z. Hu, J. Chen, D. Yan, Y. Li, H. Jia, C.-Z. Lu, Enhanced catalytic activities of MnO_x/Co_3O_4 nanocomposites prepared via MOFs-templated approach for chlorobenzene oxidation, Appl. Surf. Sci. 551 (2021) 149453.

[40] F. Lin, Z. Zhang, L. Xiang, L. Zhang, Z. Cheng, Z. Wang, B. Yan, G. Chen, Efficient degradation of multiple Cl-VOCs by catalytic ozonation over MnO catalysts with different supports, Chem. Eng. J. 435 (2022), 134807.

[41] F. Dong, W. Han, W. Han, Z. Tang, Assembling core-shell $SiO_2@Ni_aCo_bO_x$ nanotube decorated by hierarchical NiCo-Phyllisilicate ultrathin nanosheets for highly efficient catalytic combustion of VOCs, Appl. Catal. B: Environ. 315 (2022), 121524.

[42] X. Wang, W. Jiang, R. Yin, P. Sun, Y. Lu, Z. Wu, X. Weng, The role of surface sulfation in mediating the acidity and oxidation ability of nickel modified ceria catalyst for the catalytic elimination of chlorinated organics, J. Colloid Interf. Sci. 574 (2020) 251–259.

[43] Z. Zhang, J. Huang, H. Xia, Q. Dai, Y. Gu, Y. Lao, X. Wang, Chlorinated volatile organic compound oxidation over SO_4^{2-}/Fe_2O_3 catalysts, J. Catal. 360 (2018) 277–289.

[44] Y. Lao, N. Zhu, X. Jiang, J. Zhao, Q. Dai, X. Wang, Effect of Ru on the activity of Co_3O_4 catalysts for chlorinated aromatics oxidation, Catal. Sci. Technol. 8 (2018) 4797–4811.

[45] H. Song, F. Hu, Y. Peng, K. Li, S. Bai, J. Li, Non-thermal plasma catalysis for chlorobenzene removal over $CoMn/TiO_2$ and $CeMn/TiO_2$: Synergistic effect of chemical catalysis and dielectric constant, Chem. Eng. J. 347 (2018) 447–454.

[46] Q. Dai, Z. Zhang, J. Yan, J. Wu, G. Johnson, W. Sun, X. Wang, S. Zhang, W. Zhan, Phosphate-functionalized CeO_2 Nanosheets for efficient catalytic oxidation of dichloromethane, Environ. Sci. Technol. 52 (2018) 13430–13437.

[47] G. Li, K. Shen, L. Wang, Y. Zhang, H. Yang, P. Wu, B. Wang, S. Zhang, Synergistic degradation mechanism of chlorobenzene and NO over the multi-active center catalyst: The role of NO_2, Brønsted acidic site, oxygen vacancy, Appl. Catal. B: Environ. 286 (2021), 119865.

[48] H. Liu, X. Li, Q. Dai, H. Zhao, G. Chai, Y. Guo, Y. Guo, L. Wang, W. Zhan, Catalytic oxidation of chlorinated volatile organic compounds over Mn-Ti composite oxides catalysts: Elucidating the influence of surface acidity, Appl. Catal. B: Environ. 282 (2021), 119577.

[49] N. Zhang, Y. Guo, Y. Guo, Q. Dai, L. Wang, S. Dai, W. Zhan, Synchronously constructing the optimal redox-acidity of sulfate and RuO_x Co-modified CeO_2 for catalytic combustion of chlorinated VOCs, Chem. Eng. J. 454 (2023), 140391.

[50] Y. Su, K. Fu, C. Pang, Y. Zheng, C. Song, N. Ji, D. Ma, X. Lu, C. Liu, R. Han, Q. Liu, Recent advances of chlorinated volatile organic compounds' oxidation catalyzed

by multiple catalysts: Reasonable adjustment of acidity and redox properties, Environ. Sci. Technol. 56 (2022) 9854–9871.

[51] X. Lv, S. Cai, J. Chen, D. Yan, M. Jiang, J. Chen, H. Jia, Tuning the degradation activity and pathways of chlorinated organic pollutants over CeO_2 catalyst with acid sites: synergistic effect of Lewis and Brønsted acid sites, Catal. Sci. Technol. 11 (2021) 4581–4595.

[52] S. Krishnamoorthy, J.A. Rivas, M.D. Amiridis, Catalytic oxidation of 1, 2-dichlorobenzene over supported transition metal oxides, J. Catal. 193 (2000) 264–272.

[53] M. Tian, X. Guo, R. Dong, Z. Guo, J. Shi, Y. Yu, M. Cheng, R. Albilali, C. He, Insight into the boosted catalytic performance and chlorine resistance of nanosphere-like meso-macroporous $CrO_x/MnCo_3O_x$ for 1, 2-dichloroethane destruction, Appl. Catal. B: Environ. 259 (2019), 118018.

[54] B.H. Aristizábal, C. Maya, C.Md Correa, Ortho-dichlorobenzene oxidation over Pd/Co loaded sulfated zirconia and mordenite catalysts, Appl. Catal. A: Gen. 335 (2008) 211–219.

[55] J. Lichtenberger, Catalytic oxidation of chlorinated benzenes over V_2O_5/TiO_2 catalysts, J. Catal. 223 (2004) 296–308.

[56] Y. Liu, W. Wu, Y. Guan, P. Ying, C. Li, FT-IR spectroscopic study of the oxidation of chlorobenzene over Mn-based catalyst, Langmuir 18 (2002) 6229–6232.

[57] M. Angeles Larrubia, G. Busca, An FT-IR study of the conversion of 2-chloropropane, o-dichlorobenzene and dibenzofuran on V_2O_5-MoO_3-TiO_2 SCR-DeNOx catalysts, Appl. Catal. B: Environ. 39 (2002) 343–352.

[58] H. Zhao, W. Han, F. Dong, Z. Tang, Highly-efficient catalytic combustion performance of 1, 2-dichlorobenzene over mesoporous TiO_2-SiO_2 supported CeMn oxides: The effect of acid sites and redox sites, J. Ind. Eng. Chem. 64 (2018) 194–205.